HEALTH AND MEDICINE

3D organotypic skin models recapitulate autoantibody-driven pemphigus pathomechanisms and targeted therapeutic response

Haiwei Zhai[1], Xiaowei Jin[1], Amir Ostadi Moghaddam[1,2,3], Matthew F. Spieker[1], Kristina Seiffert-Sinha[4], Animesh A. Sinha[4], Ruiguo Yang[1,2,3]*, Fanben Meng[1,5]*

Copyright © 2026 The Authors, some rights reserved; exclusive licensee American Association for the Advancement of Science. No claim to original U.S. Government Works. Distributed under a Creative Commons Attribution NonCommercial License 4.0 (CC BY-NC).

Advanced three-dimensional (3D) tissue models that recapitulate autoimmune disease progression can enable mechanistic studies and accelerate the development of targeted therapies with reduced reliance on systemic immunosuppression. Here, we present a dynamic biofabrication strategy combining 3D bioprinting and cell self-organization to create multilayered skin constructs with a stratified epidermis atop a vascularized, fibroblast-remodeled dermis. This platform reconstitutes native skin architecture to model pemphigus vulgaris, an autoantibody-driven blistering disorder. Tightly reassembled keratinocytes form cell-cell adhesions that replicate pathogenic antibody–induced disruption of the epidermal barrier, while embedded vasculature and fibroblasts shape dermal barriers that regulate molecular diffusion. We demonstrate that these tissue barriers define disease phenotypes and therapeutic responses by modulating antibody and drug penetration. As proof of concept, we quantitatively evaluate epidermal growth factor receptor–targeted inhibitors by measuring individual cell-cell junction integrity and applying machine learning–assisted image texture analysis. This organotypic skin model provides a physiomimetic testbed for precise investigation of autoimmune pathogenesis and high-throughput screening of targeted therapeutic agents.

INTRODUCTION

Autoimmune diseases affect ~5% of the US population (*1*). They are commonly categorized into cell-mediated and humoral subtypes, with the latter one being driven by the aberrant production of autoantibodies targeting self-antigens. Despite their prevalence, cures for these chronic disorders remain elusive (*2*). Current treatments rely heavily on systemic immunosuppression, which often leads to severe side effects (*3*). Pemphigus vulgaris (PV), a rare but life-threatening autoimmune blistering skin disorder, exemplifies the limitations of existing therapeutic strategies. In PV, autoantibodies bind to desmosomal cadherins—primarily desmoglein-3 (Dsg3) and Dsg1—within the epidermal layers, triggering disassembly of cell-cell adhesions between adjacent keratinocytes and disrupting the epidermal barrier (*4*, *5*). Recent advances in understanding the downstream signaling pathways activated by pathogenic autoantibodies have shifted PV treatment toward more precise target-specific therapies (*6*–*10*). Inhibition of key signaling molecules such as p38 mitogen-activated protein kinase (p38 MAPK), epidermal growth factor receptor (EGFR), and phosphodiesterase 4 has shown promise in stabilizing desmosomal junctions and mitigating PV antibody–associated tissue damage (*8*, *11*–*14*). To advance the development of next-generation therapies that minimize systemic toxicity while effectively restoring tissue integrity in PV and other autoimmune disorders, it is essential to identify therapeutic targets and evaluate candidate drugs within the pathological microenvironment where affected cells originate.

Because of the limited accessibility of patient-derived tissue biopsies as ex vivo skin models, current mechanistic studies of PV pathogenesis and therapeutic screening largely depend on the traditional combination of monolayer-cultured cells and experimental mouse models (*15*). In vitro keratinocyte dissociation assays are commonly used to assess antibody pathogenicity and drug activity in monolayer cultures (*8*, *9*, *16*, *17*), while in vivo models facilitate the study of disease progression and systemic responses within complete physiological environments (*18*–*20*). However, two-dimensional (2D) keratinocyte cultures fail to replicate the structural and mechanical complexity of human epidermis, and animal studies are costly, time consuming, and often limited in their ability to capture human-specific immune responses. Moreover, most PV studies have focused on molecular mechanisms governing interactions among cell-cell junctions, pathogenic antibodies, and therapeutic agents. In contrast, the influence of autoantibody distribution and drug penetration, critical determinants of local molecular concentrations within diseased tissue (*21*, *22*), remains understudied. This gap underscores the need for advanced experimental platforms that integrate essential tissue barriers and enable precise investigation of molecular delivery and localization.

To address these challenges, bioengineered 3D tissue constructs have emerged as promising platforms for studying disease progression in vitro, combining the scalability of cell culture with the physiological relevance of animal models (*23*, *24*). Early efforts to develop skin equivalents involved 3D coculture of human keratinocytes and fibroblasts on transwell inserts to mimic the epidermis and dermis (*25*, *26*). While convenient, these models lack spatial control over each cell compartment and are limited in their ability to incorporate additional cell types, such as vasculature, in anatomically accurate locations. Emerging biofabrication techniques offer promising tools to integrate multiple cell-laden hydrogel matrices for reconstructing complex native tissues in vitro (*27*–*30*). Leveraging 3D bioprinting, multilayered skin constructs with embedded vasculature has been fabricated by precisely depositing bioinks containing diverse cell types (*31*–*33*). However, most current bioprinting technologies (*34*) fall short in reproducing the nuanced structural hierarchy and gradual layer-to-layer transitions seen in the native epidermis (*35*, *36*).

[1]Department of Mechanical and Materials Engineering, University of Nebraska-Lincoln, Lincoln, NE 68588, USA. [2]Department of Biomedical Engineering, Michigan State University, East Lansing, MI 48824, USA. [3]Institute for Quantitative Health Science and Engineering, Michigan State University, East Lansing, MI 48824, USA. [4]Department of Dermatology, University at Buffalo, Buffalo, NY 14203, USA. [5]Nebraska Center for Integrated Biomolecular Communication, University of Nebraska-Lincoln, Lincoln, NE 68588, USA.
*Corresponding author. Email: yangruig@msu.edu (R.Y.); fmeng5@unl.edu (F.M.)

To more faithfully replicate these delicate epidermal features, we developed a wound healing–inspired biofabrication approach in which reepithelialization was achieved through collective migration of keratinocytes from predefined source droplets, followed by self-initiated basal-to-suprabasal differentiation (*37*).

In this study, we introduce a dynamic biofabrication process to reassemble the native microenvironment of human skin in vitro by layering stratified epidermal sheets atop a dermis-mimicking hydrogel matrix. The self-organized keratinocytes exhibited basal-to-suprabasal transition and formed anchoring junctions, while the dermal matrix was vascularized and actively remodeled by embedded fibroblasts, establishing physical barriers that regulate molecular diffusion. Thus, this organotypic tissue model enables mechanistic probing of PV pathogenesis and effective evaluation of targeted therapies. By tracking ultrastructural alterations in cell-cell junctions across epidermal layers, we quantitatively assessed initial lesion formation induced by antibodies and examined therapeutic efficacy in stabilizing keratinocyte cohesion. Notably, by introducing pathogenic antibodies and therapeutic agents via physiologically relevant delivery routes, we explored the crucial role of dermal barriers and molecular penetration in shaping disorder phenotypes and treatment outcomes. Here, we repositioned three EGFR-targeted tyrosine kinase inhibitors (TKIs), currently approved for cancer treatment, and compared their effectiveness following topical and vascular administration. As proof of concept, we demonstrated that machine learning (ML)–driven texture analysis of tissue microsections enables automated, high-throughput assessment of therapeutic response, offering a robust tool for future drug screening.

RESULTS

Biofabrication of organotypic skin models is inspired by wound healing

As illustrated in Fig. 1, the multilayered skin architecture was dynamically reconstructed in vitro by combining 3D bioprinting with postprint guided cell self-organization. Recapitulating native skin anatomy, the organotypic model comprised stratified epidermal layers supported by a vascularized, fibroblast-laden dermal matrix. Inspired by the epithelialization process of wound healing, the epidermis was reassembled from 3D cultured keratinocytes using our recently developed approach (*37*). Specifically, fibrin (10 mg/ml)–encapsulated HaCaT cells, a widely used human keratinocyte line, were printed onto a hydrogel matrix as an array of hemispherical droplets. The interspaces between these keratinocyte source droplets were precisely defined to create geographic cues that guided collective cell migration and the formation of a confluent basal epithelial layer. These tightly packed cells expanded vertically, self-initiating basal-to-suprabasal differentiation without external stimulation (*38*). The resulting epithelial layers exhibited the typical hierarchical structure found in native epidermis (*39*).

Epidermal regeneration was supported by a dermis-mimicking matrix seeded with human dermal fibroblasts (HDFs), which was also framed with fibrin gel (10 mg/ml). Known as a provisional scaffold for wound healing, fibrin was selected for its remodelability, allowing resident stromal cells to proliferate and produce their own extracellular matrix (ECM) (*40*, *41*). To more closely replicate the dermal microenvironment, we incorporated a vascular conduit using a pin-molding method: A metal needle (outer diameter, ~310 μm) was placed as a template to create a microchannel within the 3D matrix, which was subsequently endothelialized with human umbilical vein endothelial cells (HUVECs) (*30*). The established microvessel enabled the introduction of autoimmune antibodies and therapeutic agents, mimicking in vivo molecular delivery for initiating PV pathogenesis and evaluating treatment efficacy. To accommodate multiple cellular compartments, we designed and microfabricated a customized tissue culture chamber (workflow depicted in fig. S1), with dimensions tailored to fit conventional culture dishes, such as 35-mm petri dishes and six-well plates. This customized chamber enabled precise control of the spatial and dimensional characteristics of the dermal matrix. The microvessel was positioned

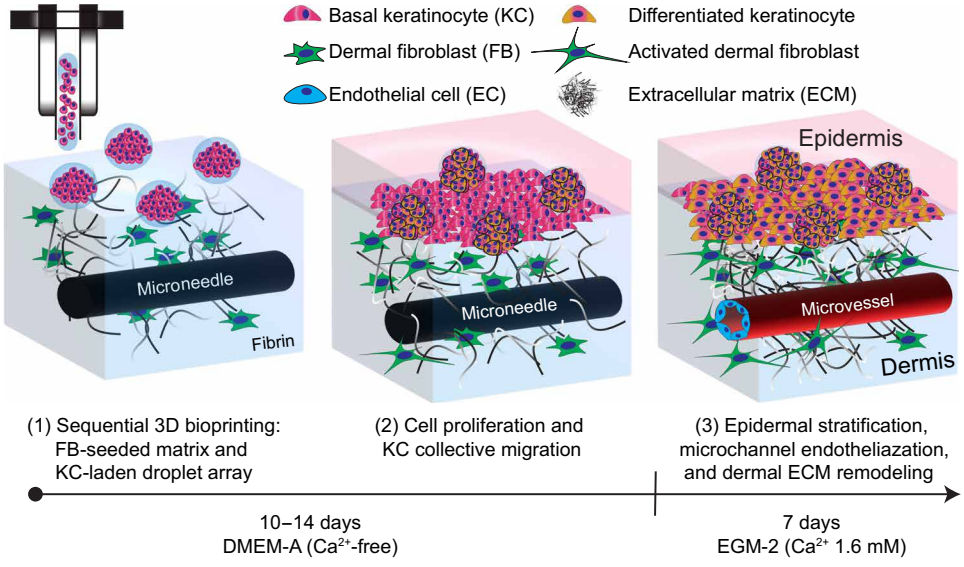


Fig. 1. 3D biofabrication of organotypic skin models. The schematic diagram illustrates the workflow of multicellular tissue construction. (1) An array of keratinocyte (KC) source droplets, spaced 2 mm center to center, is bioprinted onto a fibroblast (FB)–seeded fibrin matrix. (2) Keratinocytes proliferate and collectively migrate, forming a confluent basal layer that initiates basal-to-suprabasal differentiation. (3) Keratinocytes continue to differentiate, generating a stratified epidermis, while the microchannel is lined with endothelial cells and embedded fibroblasts actively remodel the ECM to shape the dermis.

1 mm below the matrix surface where the epidermis formed. The matrix thickness was maintained at 2 mm, consistent with the range of human dermis (~0.6 to 4 mm).

A major challenge in modeling complex physiological processes in vitro is identifying suitable coculture conditions for multiple cell types (*42*). To maintain the viability and function of all three cell types during skin tissue regeneration and maturation, we developed a stepwise culture strategy (Fig. 1). In stage I, the medium [aprotinin-supplemented Ca^{2+}-free Dulbecco's modified Eagle's medium (DMEM-A)] was optimized as Ca^{2+}-free DMEM supplemented with antifibrinolytic agent, aprotinin, to promote basal layer assembly while preserving the integrity of the dermal matrix. The Ca^{2+}-free medium maintained the basal state of HaCaT cells, supporting cell proliferation and collective migration, while elevated Ca^{2+} concentrations tend to induce keratinocyte differentiation. Aprotinin was included to counteract rapid fibrin degradation caused by HaCaT proliferation. Once a compact basal layer was formed, typically in 10 to 14 days (fig. S2), tightly packed basal keratinocytes self-initiated basal-to-suprabasal transition, as demonstrated in our previous report (*37*).

In stage II, the focus shifted to epidermal stratification, dermal matrix remodeling, and vascularization. We injected a HUVEC suspension to endothelialize the created microchannel. Low-serum (2%) endothelial cell growth medium-2 (EGM-2) medium containing a cocktail of growth factors (GFs), which included vascular endothelial growth factor (VEGF), insulin-like growth factor 1 (IGF-1), fibroblast growth factor 2 (FGF-2), and epidermal growth factor (EGF), was applied to drive vascularization and dermal matrix remodeling without impairing epidermal stratification. Ca^{2+} (1.6 mM) was reintroduced to further promote keratinocyte differentiation and to fulfill its essential role in the maturation of cell-cell adhesion. In particular, Ca^{2+} facilitates the assembly and clustering of cadherin-based junctions, especially desmosomes, which are targeted by PV antibodies. Aprotinin was removed at this stage, as HDFs became activated to remodel the surrounding matrix by gradually degrading fibrin and depositing ECM components. The skin constructs were typically matured for 7 days before modeling PV pathogenesis.

Throughout both culture stages, we dynamically measured the transepithelial electrical resistance (TEER) to monitor epidermal regeneration and functional barrier formation in these 3D skin models. A progressive TEER increase was observed, with the value eventually stabilizing at ~7-fold (fig. S3), indicating the establishment of an epidermal barrier. The initial moderate TEER increase corresponded to proliferation and collective migration of keratinocytes on the dermal matrix (early stage I), whereas the rapid rise in TEER values marked compact basal layer formation and subsequent stratification (late stage I and stage II). To facilitate nutrient exchange across the developing tissue barriers, we supplied coculture medium both via the microvessel and topically to epidermal layers (fig. S4).

Multicellular 3D models recapitulate layered skin architectures

To track the dynamic epithelization process in real time, we tagged HaCaT cells with green fluorescent protein (GFP) on E-cadherin (E-cad). The structural organization of the three cell compartments in the 3D biofabricated tissue constructs was visualized using whole-mount staining. In addition to 4′,6-diamidino-2-phenylindole (DAPI), which marks overall cell distribution, antibodies specific to platelet endothelial cell adhesion molecule 1 (also known as CD31) and α–smooth muscle actin (α-SMA) were used to label embedded HUVECs and HDFs, respectively (*43*). Stained skin models were scanned via confocal microscope, with a representative 3D reconstruction and Z-stacked top views shown in Fig. 2A. The densely packed keratinocyte layers (GFP–E-cad) formed the epidermis, covering a hydrogel matrix populated by α-SMA–stained fibroblasts and vascularized by CD31-expressing endothelial cells, mimicking the dermis. Detailed views of each cell compartment reveal that the HDF-seeded fibrin gel successfully promoted both epithelialization on the 3D matrix (Fig. 2B) and endothelialization within the microchannel (Fig. 2C). Notably, α-SMA expression was also detected in the epidermal layers, particularly in cells that had migrated from the source droplets, as well as in certain regions of the vascular conduit. This observation aligns with previous reports (*44*). While α-SMA is widely used to identify activated fibroblasts, it is also associated with increased epithelial cell motility and microvascular angiogenesis (*45*, *46*).

To further examine the multilayered architecture, we microsectioned the 3D skin models and stained the resulting tissue slices (Fig. 2D and fig. S5). Consistent with confocal imaging, keratinocytes (E-cad) were observed layering onto the fibroblast-laden (scattered DAPI signals) and vascularized (CD31-stained vessel lumen) matrix (Fig. 2D, left). Our previous study demonstrated the basal-to-suprabasal transition of self-organized epidermal layers through keratin 5 (K5; basal) and K10 (suprabasal) staining (*37*). Here, in addition to K10, the expression of involucrin (INV), an envelope precursor protein, was detected in the stratified epidermis (Fig. 2D, middle), indicating the formation of high spinous and granular layers (*47*). We quantitively assessed the epidermal thickness using higher-magnification images of representative skin models after 21 days of culture (fig. S6A). The mean thickness was measured at 45.69 μm, with some expected variation in these self-assembled epidermal layers. Compared with human epidermis (~30 μm to 1.5 mm), the layers in the 3D model fell within the physiological range but were at the thinner end, reasonable given that they had not yet developed into a fully stratified, cornified layer. Moreover, lateral tissue section views reveal ECM remodeling within the dermal matrix, as evidenced by the extensive type I collagen (COL-I) deposition (Fig. 2D, right).

Dynamic remodeling of the dermal microenvironment shapes tissue barriers

The dermal ECM serves as a physical barrier (*48*) that regulates the local accessibility of autoimmune antibodies, thereby mediating PV pathogenesis. In biofabricated skin models, fibrin matrices were remodeled, as evidenced by COL-I deposition in the microsections of 3D skin constructs. This observation prompted further investigation into how fibroblasts construct a stromal barrier that shapes the dermal microenvironment. Here, we 3D cultured HDFs within fibrin gels at a seeding density of 10^5 cells/ml using the stepwise culture approach for skin model fabrication, in which the medium was switched from DMEM-A to EGM-2 on day 7. The dermis-mimicking tissue constructs were monitored both immunohistochemically and mechanically over 2 weeks (Fig. 3, A to E).

Time-lapse confocal images were captured (Z-stacked top views in Fig. 3A) to track matrix remodeling by staining two markers: COL-I (top row) and α-SMA (bottom row), which characterize native ECM deposition and fibroblast activation, respectively. Before medium switching, HDFs exhibited minimal proliferation and slow polarization, suggesting a quiescent state. However, upon introducing EGM-2, which contains multiple GFs, HDF proliferation substantially increased, accompanied by a sharp up-regulation of both

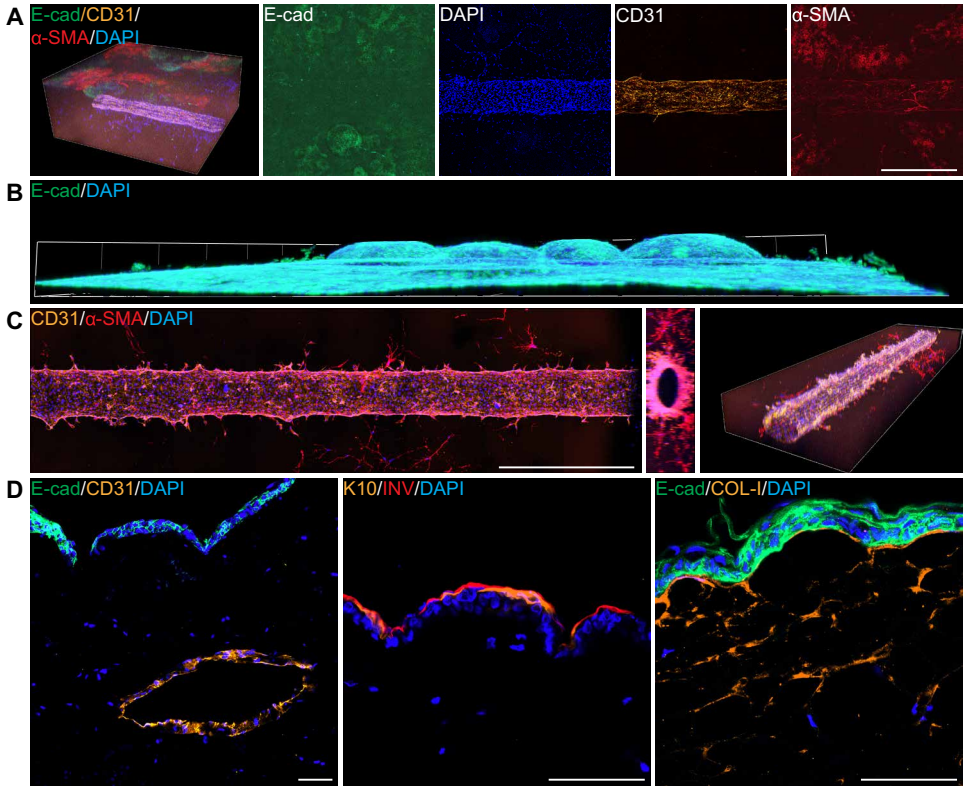


Fig. 2. Characterization of the vascularized multicellular skin model. (**A**) Confocal fluorescence images of a representative whole mount–stained skin model showing the spatial distribution of HaCaT cells, HDFs, and HUVECs (green, E-cad; blue, DAPI; orange, CD31; red, α-SMA). Scanned volume, 2.67 mm by 2.35 mm by 1.05 mm. Scale bar, 1 mm. (**B** and **C**) Panoramic scanned confocal images highlighting the self-organized epidermis (B) (scanned volume, 6.96 mm by 6.96 mm by 0.46 mm) and the vascularized dermis (C) (scale bar, 1 mm; scanned volume, 4.5 mm by 1.2 mm by 0.33 mm). (**D**) Immunofluorescence images of microsectioned tissue slices showing lateral views of the 3D skin constructs, including the distribution of cell compartments (left), stratified epidermis (middle) (red INV signals indicate differentiation into spinous and granular layers), and remodeled dermal matrix (right) (orange signals show COL-I deposition). Scale bars, 100 μm.

COL-I and α-SMA expression, indicating fibroblast activation and subsequent ECM production. IGF-1, FGF-2, VEGF, and EGF, which supplement EGM-2, have all been reported to stimulate fibroblast activity (*49*–*52*). Once activated, HDFs adopted a characteristic spindle-shaped morphology (days 7 to 14; Fig. 3A) and elongated within the 3D matrix (Fig. 3B and fig. S7). As a result, collagen fibers were gradually deposited by these fibroblasts within the dermal matrix. Furthermore, we quantitatively compared the immunofluorescent signals before and after GF introduction. The distinct slopes observed in Fig. 3C confirm that HDFs, when stimulated by these molecular factors, actively reconstructed the dermal matrix.

In parallel, we dynamically measured the viscoelasticity of HDF-laden matrices via nanoindentation. Mechanical testing demonstrated that the progressive increase in ECM components intrinsically strengthened the dermal matrix over time. While matrix stiffness remained stable during the first week, the measured complex shear modulus rapidly increased by approximately 1.5-fold from days 7 to 14 (Fig. 3D; storage and loss moduli shown in fig. S8A), suggesting matrix stiffening. The trend in mechanical measurements aligned with the immunofluorescent results, further confirming that HDFs were highly responsive to the GF cocktail stimulation and that matrix stiffening was associated with ECM deposition induced by activated fibroblasts. The strengthened dermal matrix was comparable to reported values for human dermis measured by atomic force microscopy–based nanoindentation (*53*). Notably, matrix remodeling was also influenced by the initial fibroblast density. When the seeding density was reduced by an order of magnitude, matrix stiffness exhibited only random fluctuations (Fig. 3E and fig. S8B), similar to the acellular fibrin matrix.

In addition to fibroblast-driven stromal remodeling, a microvascular conduit was integrated into the 3D skin model, establishing an endothelial barrier to regulate molecular penetration (*54*). To determine how these tissue barriers influence the delivery of autoimmune antibodies and therapeutic agents, we quantitatively measured molecular diffusion permeability by perfusing fluorescence dyes through the built-in microchannel and tracking fluorescent signals. Fluorescein isothiocyanate (FITC)–conjugated dextran (molecular weight, 150 kDa) was chosen to match the molecular weight of PV antibodies. Four parallel experimental conditions were tested to assess tissue barrier function, including (a) pure fibrin with an acellular microchannel (blank control), (b) HDF-populated matrix with an acellular microchannel (stromal barrier only), (c) pure fibrin with a HUVEC-lined microchannel (endothelial barrier only), and (d) 3D matrix containing both tissue barriers. The diffusion of FITC-dextran within different 3D matrices was tracked under a fluorescence microscope for 30 min (Fig. 3F, with time-lapse images shown in fig. S9). The permeability coefficients were then calculated by analyzing fluorescent intensity (Fig. 3G). The results demonstrated that

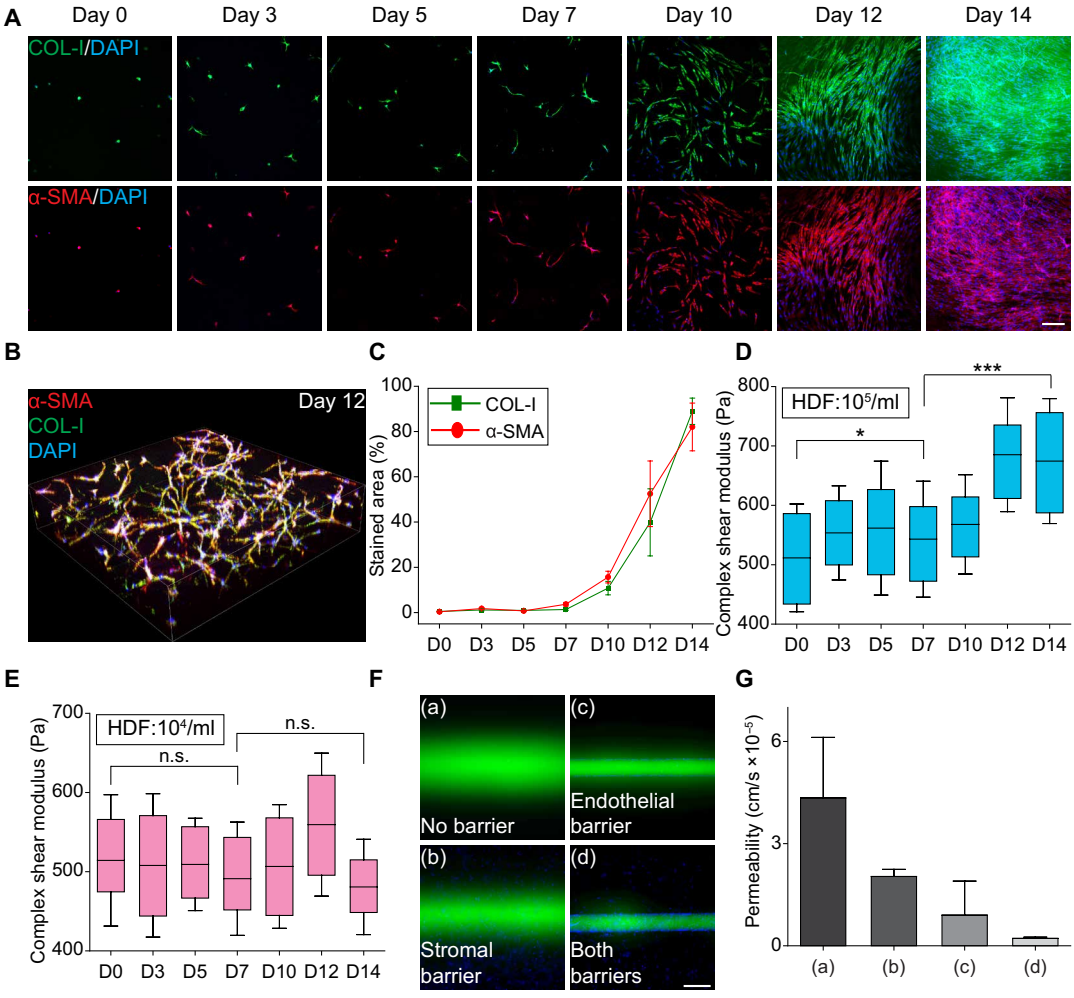


Fig. 3. Dynamic dermal barrier remolding. (**A**) Time-lapse confocal fluorescence images showing collagen deposition (top row) (green, COL I) and HDF activation (bottom row) (red, α-SMA) in fibroblast-populated fibrin matrix. Scale bar, 200 μm. (**B**) 3D reconstructed confocal image revealing the spatial distribution of HDFs and deposited ECM (COL-I) after 12 days of culture. Scanned volume, 1272.79 μm by 1272.79 μm by 242.73 μm. (**C**) Plots of biomarker-stained area versus culture time, indicating that HDFs were activated to remodel the surrounding matrix after switching to EGM-2 medium on day 7 (D7). (means ± SD, $N = 9$ fluorescence images captured from three matrices per time point). (**D** and **E**) Box plots showing time-dependent changes in the complex shear modulus of 3D matrices seeded with 10^5 cells/ml (D) (box range, 25th to 75th percentile; means ± SD, $47 \leq N \leq 71$ indentations from 12 to 18 matrices per time point; $^*P < 0.05$ and $^{***}P < 0.001$; day 7 versus day 0, $P = 0.049$; day 14 versus day 7, $P < 0.001$) and 10^4 cells/ml (E) [box range, 25th to 75th percentile; means ± SD, $12 \leq N \leq 24$ indentations from three to six matrices per time point; $P > 0.05$, not significant (n.s.); day 7 versus day 0, $P = 0.307$; day 14 versus day 7, $P = 0.603$]. (**F**) Fluorescence images showing the diffusion of fluorescently labeled dextran (150 kDa) in various dermal-mimicking matrices after 30-min perfusion: (a) pure fibrin (10 mg/ml) with an acellular microchannel, (b) HDF-populated matrix with an acellular microchannel, (c) pure fibrin with a HUVEC-lined microchannel, and (d) matrix containing both cell compartments (green, dextran; blue, DAPI). Scale bar, 500 μm. (**G**) Bar charts of calculated permeabilities, quantitatively demonstrating the impact of tissue barriers on molecular diffusion (means + SD, $3 \leq N \leq 7$).

both stromal remodeling and endothelialization restricted molecular transport from the microchannel to the surrounding matrix. Notably, when both barriers coexisted, closely mimicking native microenvironments, molecular diffusion was most limited, with a permeability coefficient of 2×10^{-6} cm/s for 150-kDa dextran, ~20 times lower than the pure fibrin matrix. Collectively, these detailed characterizations of dynamically biofabricated skin equivalents demonstrate that the developed in vitro tissue constructs not only provide cellular targets for autoimmune antibodies and therapeutic candidates but also establish physiomimetic transport routes, closely recapturing molecular penetration dynamics in local skin microenvironments.

Pathomimetic skin models reflect adhesion disruption in PV

PV pathogenesis is widely recognized to be triggered by autoantibodies that target and dissociate desmosomal junctions in the epidermis (*4*, *5*). While experimental models using human skin organ culture mimic the disorder by topically applying PV-associated antibodies to the epidermis (*16*, *55*, *56*), the organotypic skin construct we developed integrates a vascularized dermal matrix, allowing the physiological dissemination of autoantibodies from blood vessels to the epidermis to be recapitulated. To explore how the dermal microenvironment and molecular transport influence epidermis-antibody interactions in PV pathogenesis, we introduced pathogenic antibodies

through two administration routes (Fig. 4A): (i) topical addition, as in conventional PV models, and (ii) vessel perfusion, where antibodies were injected via the built-in microvessel to mimic in vivo delivery. As in previous studies, the commercially available anti-Dsg3 antibody (AK23) was used to disrupt desmosomes (*17*, *37*, *57*). While untreated models served as healthy controls, two concentrations of AK23 (10 and 50 μg/ml) were tested to evaluate dose-dependent effects on cell-cell junction dissociation.

After 24 hours of treatment, tissue constructs representing each test condition were cryosectioned to examine the effects of antibody attack. As shown in representative images (Fig. 4B and fig. S10), AK23 and Dsg3 were sequentially immunostained to visualize PV antibody distribution (top row) and desmosomes at epidermal layers (middle row), while GFP–E-cad images (bottom row) were captured to highlight cell boundaries in keratinocytes. Under the four treatment conditions, the skin constructs exhibited distinct phenotypes, with (*) indicating regions of complete Dsg3 loss and (dashed arrowheads) marking locations with nonjunctional or partially absent Dsg3, corresponding to antibody distribution. To assess the interactions between pathogenic antibodies and their antigens at cell-cell junctions, we quantified the AK23 fluorescence intensity (Fig. 5A) and spatial colocalization of AK23 and Dsg3 (Fig. 5B). To correlate initial PV pathogenesis and the resulting phenotypes with antibody penetration, we evaluated the disorganization of cell-cell junctions that stabilize different epidermal layers. As defined in Fig. 5C, targeted junctions were categorized on the basis of their epidermal locations: (i) basal to basal, (ii) basal to suprabasal, and (iii) suprabasal to suprabasal. Full width at half maximum (FWHM; definition shown in fig. S11) values of Dsg3 and E-cad signals between neighboring keratinocytes were measured to represent the mean width of desmosomal and adherens junctions (Fig. 5, D to I), with higher values indicating more severe junction dissociation.

When the epidermis was directly exposed to antibodies at both concentrations via topical addition, AK23 signals were detected throughout the stratified epidermal layers (Fig. 4B, top row) and largely colocalized with Dsg3 {Fig. 5B, T10 [topical addition of

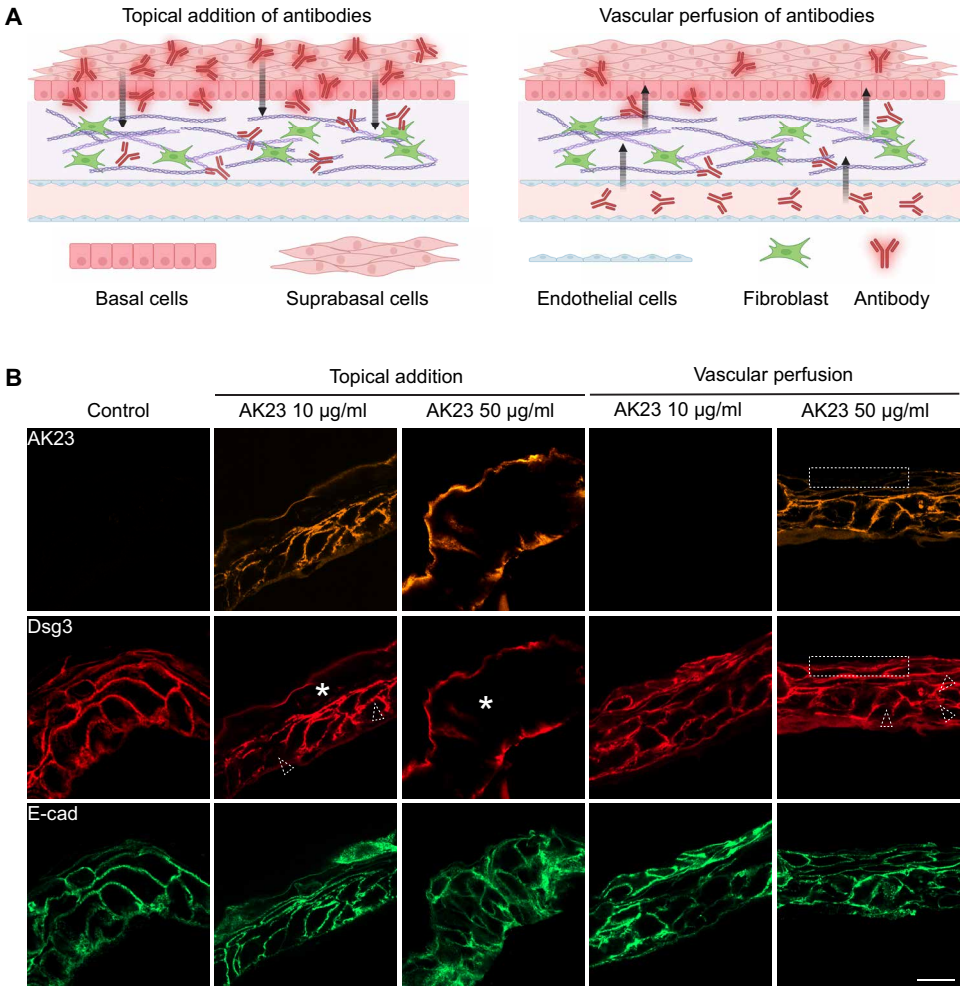


Fig. 4. Recapitulation of initial PV pathogenesis in the 3D model. (**A**) Schematic illustrating two administration routes of PV antibodies: topical addition (left) (AK23 was directly applied onto the epidermis) and vascular perfusion (right) (AK23 was injected via the microvessel and traveled through the dermis). (**B**) Confocal images of immunostained tissue microsections from PV models after antibody treatments: untreated control, topical addition of AK23 (10 and 50 μg/ml), and vascular perfusion of AK23 (10 and 50 μg/ml), showing the bound AK23 (orange) and epidermal cell-cell junctions (red, Dsg3; green, E-cad). Asterisks (*) mark regions of complete Dsg3 loss; dashed arrowheads indicate nonjunctional or partially absent Dsg3. Dashed rectangles highlight incomplete AK23 penetration due to dermal barriers. Scale bar, 20 μm.

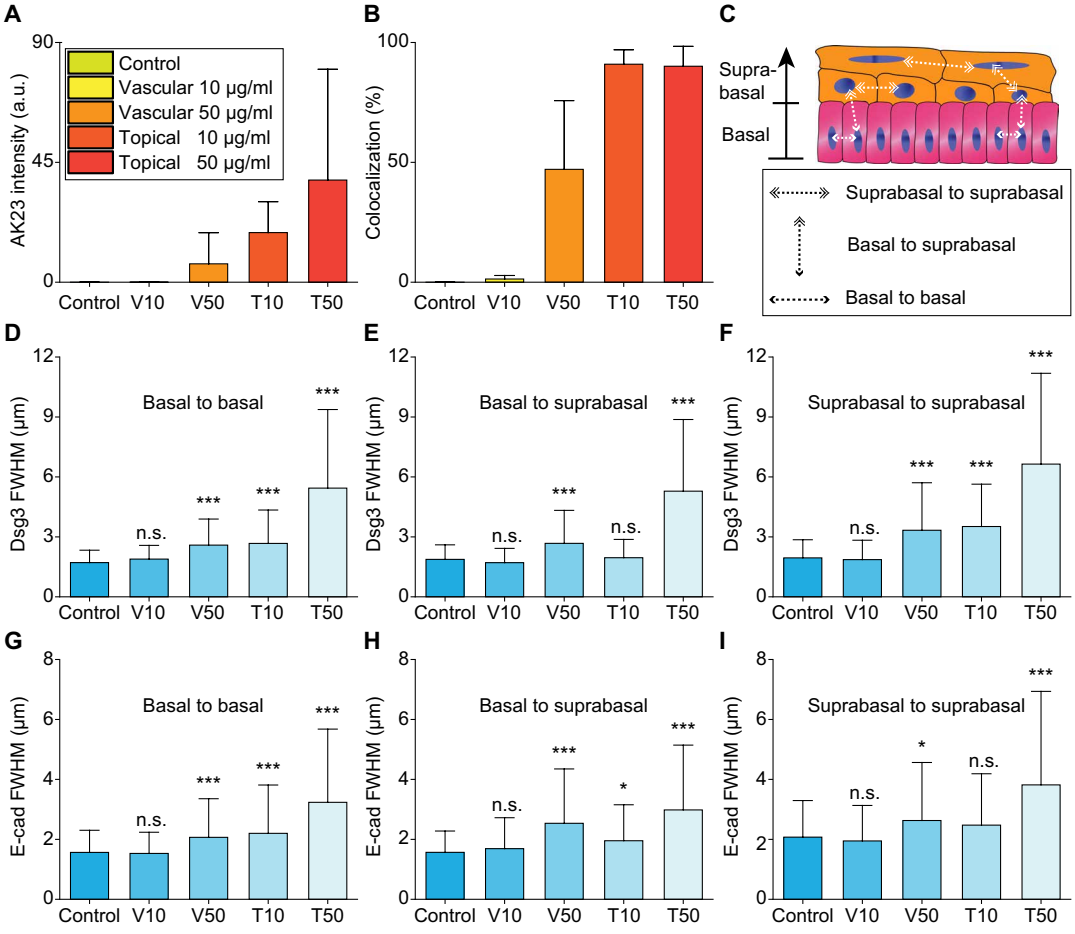


Fig. 5. Pathological alterations of cell-cell adhesions. (**A** and **B**) Bar charts showing AK23 intensity detected in the epidermal layers (A) and the colocalization ratio of AK23 and Dsg3 (B), indicating the impact of dermal barriers on antibody penetration. Means + SD, $12 \leq N \leq 39$ tissue slice images from three to nine skin models). a.u., arbitrary units. (**C**) Schematic illustrating the categorization of cell-cell junctions based on their epidermal location: basal to basal, basal to suprabasal, and suprabasal to suprabasal (red, basal cells; orange, suprabasal cells). (**D** to **I**) Bar graphs showing the measured junction width (quantified by FWHM values) of Dsg3 [(D) to (F)] and E-cad [(G) to (I)] in response to AK23 binding at each epidermal location. Means + SD, $21 \leq N \leq 196$ cell-cell junctions measured from six to nine skin models; $P > 0.05$ (not significant), $^{*}P < 0.05$, and $^{***}P < 0.001$, compared with the untreated control; (D) V10, $P = 0.081$; V50, T10, and T50, $P < 0.001$; (E) V10, $P = 0.222$; T10, $P = 0.524$; V50 and T50, $P < 0.001$; (F) V10, $P = 0.702$; V50, T10, and T50, $P < 0.001$; (G) V10, $P = 0.766$; V50, T10, and T50, $P < 0.001$; (H) V10, $P = 0.456$; T10, $P = 0.018$; V50 and T50, $P < 0.001$; (I) V10, $P = 0.672$; V50, $P = 0.039$; T10, $P = 0.087$; T50, $P < 0.001$.

antibodies (10 μg/ml)]/T50 bars}. Accordingly, desmosomal junctions were readily disrupted, as indicated by increased FWHM values (Fig. 5, D to F, T10/T50 bars). Nonjunctional Dsg3 was then internalized and degraded, resulting in local and regional loss of these desmosomal cadherins (Fig. 4B and fig. S10, middle row). The extent of Dsg3 dissociation was positively correlated with AK23 concentration. In models treated with a high concentration of AK23, total loss of Dsg3 throughout the epidermis was observed in some cases, leading to a substantial drop in fluorescence intensity and contributing to the wide data distribution of T50 bars in Fig. 5 (A and D to F). Notably, basal-to-suprabasal junctions remained unaffected at the lower AK23 concentration (Fig. 5E, T10 bar), possibly due to a lipid barrier formed in the top suprabasal layers. This is consistent with epidermal differentiation staining (Fig. 2D, middle), where INV expression, a marker of the upper stratum granulosum (*58*), was detected. Thus, in addition to directly interacting with the top suprabasal layers, AK23 first reached the basal layer via the hydrogel matrix and subsequently diffused into adjacent suprabasal layers.

We also show that vascular perfusion of AK23 at the higher concentration led to antibody penetration into the epidermal layers (Fig. 4B, top row), indicating that our model is able to recapitulate the physiological diffusion of autoantibodies from the vasculature, through the dermis, and into reach the epidermis. Although AK23 specifically targets Dsg3, its access was markedly restricted by the intrinsic barrier function of the dermal stroma when comparing vessel injection to topical application, as indicated by substantially reduced fluorescence intensity (Fig. 5A). When antibodies were delivered via the microvascular channel and traveled through the endothelium and dermal matrix, a much lower concentration of AK23 reached the epidermis. This was evident in the 10 μg/ml–treated group, where AK23 was barely detectable (Fig. 5, A and B) and no junction disassembly was observed. Only in skin models treated with the higher AK23 concentration (50 μg/ml) did antibodies reach an effective level, primarily accumulating in the basal and lower suprabasal layers (compare dashed rectangle areas in the top and middle rows of Fig. 4B). Consequently, Dsg3 dissociation was captured in

these layers, as indicated by dashed arrows in Fig. 4B and elevated FWHM values {V50 [vascular perfusion of antibodies (50 μg/ml)] bars in Fig. 5, D to F}. To further clarify the role of dermal barriers in junction disruption at the epidermis, we performed a control experiment using skin models with more permeable dermal matrices, in which a low density of HDFs (10^4 cells/ml) was seeded. As demonstrated in fig. S12, even an AK23 (10 μg/ml) treatment was sufficient to disrupt desmosomes under these conditions.

In addition to using E-cad to indicate keratinocyte distribution and boundaries, we examined their junction integrity (Fig. 5, G to I), as alterations in these adherens junctions have been associated with PV progression (*59*). While E-cad junction widths exhibited a trend similar to Dsg3-containing junctions in response to AK23 treatment, the measured FWHM values showed only slight increases, and no visible E-cad loss was detected. Keratinocyte-expressed E-cad signals were readily detected in the epidermal layers across all antibody-treated conditions (Fig. 4B, bottom row). This suggests that the complete regional loss of Dsg3 observed following direct epidermal exposure to antibodies (Fig. 4B, middle row) does not equate to physiological blister formation. Although less severe cell-cell adhesion disorder was detected when AK23 traveled through the dermis (V50 versus T50 in Fig. 5, D to F), the distribution and targeted regions of the pathogenic antibodies more closely recapitulate the pathological microenvironment of PV. Specifically, desmosomal junction disruption primarily localized to the basal and immediate suprabasal layers of the deeper epidermis, consistent with observations in patients with PV (*4*, *5*, *60*).

Together, these results highlight the critical role of the dermal microenvironment in skin disease modeling, particularly the influence of molecular penetration routes in autoantibody-mediated disorders. The 3D skin model presented here precisely recaptures the initial pathogenic features of the autoimmune disease, providing a robust in vitro platform for testing therapeutic agents.

Targeted therapeutic agents are repositioned for PV management

PV antibody–mediated transactivation of EGFR contributes to the dissociation of keratinocyte cell-cell adhesion (*10*). As illustrated in fig. S13, PV antibody binding induces activation of the p38 MAPK and proto-oncogene tyrosine-protein kinase Src pathways, which, in turn, can activate EGFR in a ligand-independent manner. Activated EGFR is associated with Dsg3 endocytosis, desmosomal plaque destabilization, and keratin retraction, collectively leading to loss of cellular adhesion. Evidence shows that EGFR inhibition via TKIs stabilizes desmosome assembly in monolayer-cultured keratinocytes and mouse models, suggesting EGFR as a potential target for PV management (*8*, *12*, *13*). To demonstrate the feasibility of our 3D organotypic skin models in screening targeted therapeutic agents, we selected three small-molecule TKIs to suppress EGFR activity, thus mitigating PV antibody–induced cell-cell adhesion disorders: (i) osimertinib, a third-generation EGFR inhibitor specifically targeting mutations in exon 20 (T790M), exon 21 (L858R), and exon 19 deletions (*61*); (ii) lapatinib, a first-generation TKI cotargeting EGFR and human epidermal growth factor receptor 2 (HER2) (*62*); and (iii) brigatinib, a second-generation anaplastic lymphoma kinase (ALK) inhibitor with activity on EGFR mutations (*63*). As illustrated in fig. S14, EGFR-targeted inhibitors were administered via two parallel routes: (i) topical addition and (ii) vessel perfusion.

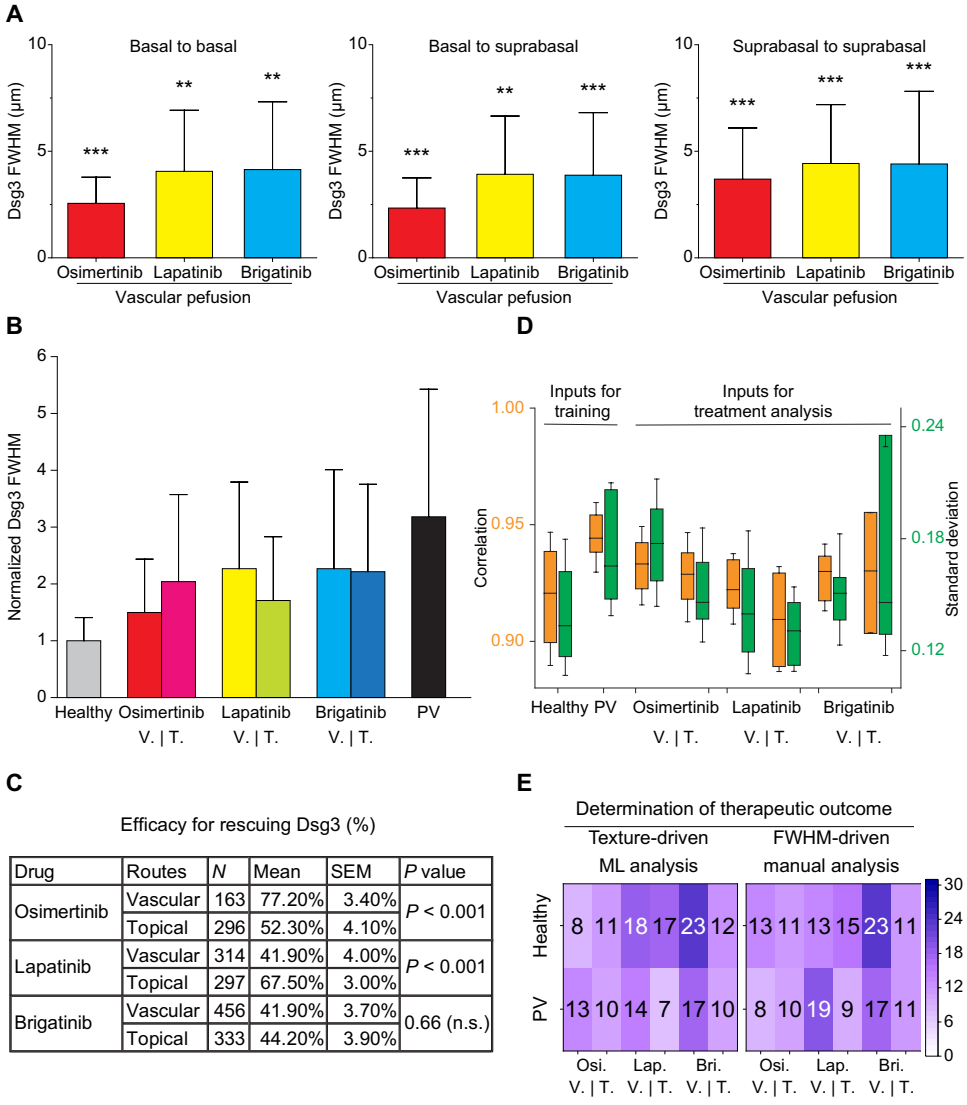
To quantitatively assess the efficacy of each therapeutic agent, we evaluated desmosome integrity in the epidermal layers of 3D skin models using FWHM measurements of Dsg3. Junctional disruption was triggered by applying AK23 (50 μg/ml) directly to the epidermis, creating the most severe Dsg3 dissociation (Figs. 4 and 5), where split junctions (mean FWHM, 6.10 μm) were distinguishable from intact ones (mean FWHM, 1.98 μm). The 3D skin equivalents were incubated with pathogenic antibodies and TKIs for 24 hours before tissue microsections were examined. Untreated skin constructs served as healthy controls, while PV disease controls were generated by applying only AK23 to 3D models.

Tissues slices from TKI-treated PV models were stained to quantify the width of Dsg3-containing junctions (representative fluorescence images shown in fig. S15). Similar to dissociation characterization, junctions were categorized into basal to basal, basal to suprabasal, and suprabasal to suprabasal. The measured FWHM values are shown in Fig. 6A and fig. S16, when therapeutic agents were introduced via the built-in microvessel and direct epidermal application, respectively. Targeted treatments through both administration routes substantially reduced junction width across epidermal layers compared to PV disease controls, indicating that EGFR inhibitors stabilized desmosomes despite antibody binding.

First, TKI-induced Dsg3 rescue and the impact of drug transport routes were assessed quantitatively by comparing individual junctions (Fig. 6B), with treatment efficacy determined by FWHM alterations (Fig. 6C). Desmosomal junctions maintaining integrity at an FWHM of 1.98 μm were considered 100% effective, while junction width reaching 6.10 μm indicated complete dissociation induced by antibodies (0% effectiveness). As depicted in Fig. 6C, osimertinib delivered via the microvessel and lapatinib applied directly to the epidermis were most effective in stabilizing Dsg3-containing junctions, with efficacies of 77.2 and 67.5%, respectively. Brigatinib, which primarily targets ALK, showed ~40% efficacy, the lowest among the three inhibitors and independent of administration routes. However, drug transport pathways substantially influenced the efficacy of the other two TKIs. Travel through the dermal matrix promoted osimertinib-induced Dsg3 rescue but limited lapatinib's action, resulting in a 25% efficacy difference for both drugs. These findings emphasize the critical role of dermal microenvironments in shaping epidermal drug responses, an aspect often overlooked in conventional preclinical models.

ML-assisted analysis is introduced to enhance screening throughput

To demonstrate the potential of these organotypic skin models for high-throughput therapeutic screening, which often requires analysis of thousands of tissue specimens, we developed an ML-assisted approach to automatically assessing fluorescence-stained microsections, slice by slice. Texture features derived from the gray-level co-occurrence matrix (GLCM) analysis served as inputs for the ML model (*64*). Specifically, correlation and SD, which measure image linearity and variation in intensity values, were calculated to classify tissue slices (Fig. 6D). The ML model was trained with these texture parameters from two control groups to define outcome categories: "healthy" and "PV," indicating effective and ineffective therapies, respectively. Tissue slices from each TKI-treated skin model were quantitatively analyzed, and therapeutic efficacy was assessed using a Random Forest algorithm (*65*). For each treatment, 20 to 40 tissue



Drug	Routes	*N*	Mean	SEM	*P* value
Osimertinib	Vascular	163	77.20%	3.40%	$P < 0.001$
	Topical	296	52.30%	4.10%	
Lapatinib	Vascular	314	41.90%	4.00%	$P < 0.001$
	Topical	297	67.50%	3.00%	
Brigatinib	Vascular	456	41.90%	3.70%	0.66 (n.s.)
	Topical	333	44.20%	3.90%	

Fig. 6. Therapeutic effect of the EGFR-TKIs. (**A**) Bar graphs showing the measured FWHM of Dsg3-containing junctions stabilized by the vascularly delivered TKIs [osimertinib (Osi.), lapatinib (Lap.), and brigatinib (Bri.)] at different epidermal locations in the PV models. Means + SD, 38 ≤ *N* ≤ 160 cell-cell junctions measured from 21 to 40 tissue slice images from three to four PV models; $^{**}P < 0.01$ and $^{***}P < 0.001$, compared with the PV controls induced by topical addition of AK23 (50 μg/ml); basal to basal: osimertinib, $P < 0.001$; lapatinib, $P = 0.0022$; brigatinib, $P = 0.0011$; basal to suprabasal: osimertinib and brigatinib, $P < 0.001$; lapatinib, $P = 0.0011$; suprabasal to suprabasal: osimertinib, lapatinib, and brigatinib, $P < 0.001$. (**B** and **C**) Quantitative comparison of EGFR-targeted therapies based on FWHM measurements of individual Dsg3-containing junctions: (B) bar chart showing average desmosome width across epidermal layers, normalized to the healthy controls (without AK23 exposure), under topical (T.) versus vascular (V.) TKI administration (means + SD, 163 ≤ *N* ≤ 526 cell-cell junctions measured from 21 to 45 tissue slice images from three to nine PV models); (C) treatment efficacy calculated as the relative change in FWHM, demonstrating the influence of drug delivery route on therapeutic outcomes. (**D** and **E**) ML-assisted image analysis of tissue microsections to evaluate TKI efficacy: (D) GLCM-derived texture parameters (orange, correlation; green, SD), extracted from control and TKI-treated groups, were used to train the ML model and assess therapeutic effectiveness (box range, 25th to 75th percentile; means ± SD, 21 ≤ *N* ≤ 45 tissue slice images from three to nine PV models); (E) the resulting classification matrix was compared with manual scoring outcomes, where therapy was defined as effective if ≥45% of desmosomal junctions retained structural integrity.

slices collected from multiple skin models were examined (the sample sizes used for ML model training and treatment prediction are provided in table S1). As shown in the outcome matrix (Fig. 6E), ~40 to 70% of slices were classified as healthy by the automatic analysis, where TKIs effectively rescued desmosomes.

To validate the ML-assisted method, we manually examined tissue slices to count integrated versus disrupted desmosomes. Junctions with an FWHM of ≤2.67 μm were classified as normal desmosomes, while those with an FWHM of ≥3.04 μm were considered dissociated. These boundaries were set on the basis of a *z*-score of ±0.674, corresponding to a 50% probability. The ratio of normal to total junctions per tissue slice was calculated (table S2), and a slice was classified as healthy if this ratio met a defined threshold. The agreement between automated and manual analysis was statistically tested using Cohen's kappa coefficient (κ) (*66*). ML-assisted analysis showed the highest concordance with FWHM-driven manual assessment

when a 45% threshold was used to define drug effectiveness (Fig. 6E), yielding a κ value of 0.836, indicative of near-perfect agreement ($\kappa > 0.8$). This outperformed thresholds of 40, 50, 30, and 60%, which generated κ values of 0.782, 0.726, 0.589, and 0.462, respectively, suggesting substantial ($0.6 < \kappa \leq 0.8$) and moderate ($0.4 < \kappa \leq 0.6$) agreement (fig. S17). Thus, the developed ML-assisted approach provided a rigorous and automated assessment of therapeutic effects on microsectioned tissue slices. By combining programmable fabrication of tissue equivalents with ML-driven imaging analysis, this organotypic model platform offers a promising tool for prioritizing and repositioning therapeutic agents in a high-throughput manner.

DISCUSSION

In this study, we bioengineered organotypic tissue architectures that comprised both stratified epidermal layers and vascularized, continuously remodeled dermal matrices (Figs. 2 and 3), closely resembling the physiological microenvironment of human skin. Methodologically, the biofabrication process, inspired by wound healing, integrates 3D bioprinting with cell self-organization under programmable tissue culture. Structurally, tightly packed keratinocyte layers reassembled an epidermis exhibiting hierarchical basal-to-suprabasal differentiation. The fibroblast-remodeled fibrin matrix matched the native dermis both chemically (*67*) and biomechanically (*53*), while embedding a microvessel lined by endothelial cells, allowing for physiological molecular delivery.

Relative to previously established organotypic skin equivalents, our 3D bioengineered multicellular construct offers several advantages for in vitro disease modeling: (i) Ex vivo patient skin cultures retain native architecture but are constrained by their limited accessibility, as repeated biopsies of the same lesion through disease progression are impractical (*55*, *56*). By contrast, our 3D skin constructs are programmably biofabricated, allowing reproducible generation and scalable adaptation for high-throughput testing. (ii) Transwell-based full-thickness skin models typically accommodate only keratinocytes and fibroblasts and lack a functional endothelial barrier (*25*, *26*). Our constructs, in contrast, are vascularized, with epidermal, stromal, and endothelial compartments precisely arranged to mimic physiological organization. (iii) Skin-on-a-chip platforms rely on patterned microchannels to compartmentalize cell populations, with tissue layers often separated by porous membranes or chamber walls (*68*), which do not recapitulate native architecture. In our models, all cell types are directly integrated within a continuous hydrogel matrix, closely mimicking their intercellular interactions in vivo. (iv) 3D bioprinted skin models are limited by printing resolution, hindering the faithful construction of tens-of-micrometer epidermal layers with basal-to-suprabasal transitions (*31*–*33*). In contrast, reepithelialization in our skin constructs arises from keratinocyte collective migration and self-organized differentiation, whereby a tightly packed basal layer naturally establishes cell-cell adhesions and stratification, preserving epidermal integrity and hierarchy. This dynamic process mirrors aspects of wound healing, providing a specialized platform to investigate how autoimmunity affects tissue regeneration, a capability beyond that of existing models.

Functionally, the tightly packed HaCaT cells formed desmosomal junctions enriched with Dsg3, the primary autoantigen in PV. Beyond existing PV models, our system incorporated an HDF-remodeled fibrin matrix and a HUVEC-aligned microchannel to establish dermal tissue barriers (Fig. 3), enabling the study of autoantibody penetration in PV pathogenesis, an often-overlooked factor in autoimmune disease research (*22*). The epidermal, stromal, and endothelial barriers collectively regulated molecular diffusion and distribution, thereby shaping epidermal phenotypes following antibody treatment (Fig. 4). These biofabricated 3D models offer a substantial advantage over in vivo and ex vivo systems in probing tissue penetration of functional molecules, as the dimensional and spatial characteristics of their epidermal and dermal compartments can be precisely defined. Progressive collagen deposition and enhanced ECM mechanical properties limited pathogenic antibody access to cell-cell adhesions in epidermis (Fig. 5). The tested AK23 concentrations aligned with serum levels of Dsg3-specific immunoglobulin Gs in patients with PV (*69*). Only when an effective AK23 concentration accumulated was desmosome disruption initiated at the basal and adjacent suprabasal layers, consistent with clinical observations of PV antibody primarily binding in the deep epidermis (*4*, *60*). Together, this finding underscores the critical role of microenvironmental factors in PV pathogenesis and suggests an alternative direction for PV management by restricting autoantibody penetration.

These pathomimetic models functioned as in vitro testbeds for therapeutic candidates (Fig. 6). While systemic corticosteroids and immunosuppressants remain the mainstay of PV management (*70*), emerging strategies target downstream signaling pathways activated by autoantibodies, such as p38 MAPK, cyclic adenosine monophosphate, and EGFR (*8*, *11*), to stabilize keratinocyte adhesion. Among these signaling molecules, EGFR has been extensively studied (*8*). Three generations of small-molecule TKIs have been approved by the Food and Drug Administration for cancer treatment with robust pharmacological and biosafety assessments (*71*). Recent studies demonstrated that first-generation TKIs (erlotinib, lapatinib, and gefitinib) restore desmosome ultrastructure by suppressing EGFR activity in monolayer-cultured keratinocytes and mouse models (*8*, *12*, *13*). Using our skin model, we extended drug repurposing to newer inhibitors and assessed administration route impacts on treatment efficacy. The vascularized tissue construct enabled therapeutic agent perfusion via the built-in microvessel, closely mimicking their physiological delivery, as these small-molecule drugs are primarily designed for oral administration.

In addition to lapatinib, which was reported previously, brigatinib and osimertinib also stabilized desmosomal adhesion upon AK23 binding. However, therapeutic efficacy and administration route dependency varied among the three EGFR-TKIs (Fig. 6, B and C). While lapatinib, which inhibits overexpressed EGFR and HER2 in tumor cells (*62*), effectively prevented Dsg3 dissociation as previously reported, its efficacy declined when delivered vascularly, likely due to off-target binding in dermal fibroblasts that also express wild-type EGFR (*72*). Brigatinib, a dual ALK/EGFR inhibitor selective for EGFR mutants (*63*), exhibited route-independent effects but relatively lower efficacy in desmosome stabilization, owing to the weak affinity to wild-type EGFR. Unexpectedly, osimertinib, a third-generation EGFR inhibitor primarily targeting mutant EGFR forms, showed superior treatment effects when injected via the built-in microvessel. In this setting, the dermal matrix acted as a molecular sink, suggesting a low-dose preference for osimertinib in stabilizing desmosomal junctions. Although the mechanism remains unclear, supporting evidence includes the following: (i) Osimertinib effectively regulates receptor tyrosine kinase activity in keratinocytes, such as HaCaT, despite its preference for EGFR mutations over wild types in cancer treatment (*73*); and (ii) an animal study revealed a nonlinear V-shaped

dose-response curve for EGFR inhibition in epidermal blistering (*12*), with proteomic analysis of HaCaT cells linking osimertinib to apoptotic signaling and DNA damage (*74*). These drug testing results highlight the potential of our pathomimetic models for therapeutic screening as well as optimization of agent dose and administration strategies for PV treatment. Moreover, the route-dependent efficacy of each therapeutic agent suggests that delivery of small-molecule TKIs could move beyond the conventional oral route and be achieved through advanced wearable devices, such as microneedle-array skin patches, to enable precise, localized administration by topical or intralesional means (*75*).

A key advantage of bioengineered organotypic models is their ability to bridge the scalability of in vitro cell tests with the physiological complexity of ex vivo and in vivo studies. We further demonstrated their potential in high-throughput screening by integrating ML-assisted automated analysis of skin model microsections. A κ value of >0.8 indicated near-perfect agreement between ML-driven image texture analysis and the manual measurements of Dsg3-containing desmosomal junctions using FWHM values (Fig. 6, D and E), although inconsistencies in treatment efficacy evaluation were detected. The current ML method examines entire fluorescence images slice by slice, whereas manual measurements focus on individual junctions. Future improvements will optimize ML models by incorporating additional texture features linked to cell-cell adhesions.

Our organotypic tissue models closely mimic both prelesional and perilesional skin in PV, including antibody-induced Dsg3 disruption. However, an intraepidermal split, which leads to blister formation in patient skin, did not fully develop. This may be attributed to several factors. First, the 3D models underwent only a single cycle of AK23 antibody treatment, whereas in vivo, keratinocytes are chronically exposed to autoantibodies. In addition, HaCaT cells often express higher levels of Dsg1 than normal human epidermal keratinocytes (*15*), which may compensate for the loss of Dsg3 in desmosomal junctions and prevent complete detachment of the epidermal layers. Moreover, tangential or lateral pressure within the tissue environment is typically required to dislodge suprabasal layers in perilesional skin, a clinical pemphigus feature known as the Nikolsky sign (*76*). Thus, future improvements to model functionality could include adjusting the dose or frequency of antibody treatments, replacing HaCaT cells with primary keratinocytes, and applying controlled mechanical and/or fluidic stress to the epidermis. While the current study primarily examined acute-phase responses following PV antibody attack, the organotypic model system could be further advanced, through optimized long-term culture conditions and integration of in situ biosensors for real-time monitoring, to more accurately recapitulate cyclical healing and remission phases characteristic of chronic autoimmune skin diseases.

While the current 3D constructs incorporate the three most essential skin cell compartments, they do not yet fully replicate the complexity and heterogeneity of native skin. Planned structural optimizations include the following: (i) expanding the vascular network, transitioning from a uniaxial microvessel to a multiscale microcirculatory system via chemically guided sprouting angiogenesis, as developed in our previous studies (*30*); (ii) enhancing epidermal differentiation, establishing an air-liquid interface to promote cornified layer formation (*77*) by refining the culture chamber design; (iii) modeling local immune dysregulation, introducing PV-associated immune cells, including $CD4^+$ T cells and B cells, through the built-in vasculature to mimic their targeted infiltration and subsequent aggregation within the skin lesions; (iv) personalizing disease models, incorporating patient-derived keratinocytes and patient-specific PV autoantibodies to more accurately capture individual disease conditions and improve clinical relevance. The programmable strategy developed here may enable the adaptation of varied culture conditions to accommodate multiple primary cells.

In summary, we report a 3D bioprinting–mediated approach for assembling hierarchical skin equivalents in vitro, aiming to bridge gaps between conventional cell (co)cultures, experimental animal models, and ex vivo patient tissue slices. These models were applied to study PV pathomechanisms and test EGFR-targeted therapies, emphasizing the critical role of molecular transport in disease phenotypes and therapeutic outcomes. The integration of programmable model construction with ML-facilitated tissue analysis offers the potential of high-throughput screening and repositioning therapeutic agents. Together, these results establish a foundation for future studies to unravel autoimmune cascades and guide effective management strategies. Moving forward, we will enhance the structural complexity of the skin equivalent, model chronic disease progression, and refine ML algorithms for ultrastructural analysis. In the longer term, the pathomimetic system will be advanced to dissect PV signaling and autoimmune cascades, while preclinical efforts will establish personalized testbeds for evaluating patient-specific therapies and assessing innovative drug delivery devices.

MATERIALS AND METHODS

Cell maintenance

GFP–E-cad–HaCaT cells, prepared following a previously developed method (*37*), were cultured in Ca^{2+}-free DMEM (21068028, Thermo Fisher Scientific) supplemented with 10% fetal bovine serum, 1% GlutaMAX, and 1% penicillin-streptomycin. HUVECs (C2519A, Lonza) and HDFs (CC2511, Lonza) were maintained in EGM-2 BulletKit (CC-3162, Lonza) and FGM-2 Fibroblast Growth Medium-2 BulletKit (CC-3132, Lonza). All cells were incubated at 37°C supplied with 5% CO_2.

Tissue culture chamber fabrication

Culture chambers were fabricated by casting polydimethylsiloxane (PDMS; SYLGARD 184, Dow Inc.) into a customized mold 3D printed using a PolyJet printer (Objet500 Connex 3, Stratasys). The workflow is illustrated in fig. S1 (steps 1 to 6). A 1.5-inch-long (3.81-cm-long), 30-gauge needle was placed into the mold before pouring the PDMS to template the inlet and outlet of the culture chamber. After curing, the needle was removed from the mold. The resulting PDMS chamber was then detached from the mold and bonded to an oxygen plasma–treated substrate (either a coverslip or a silicone sheet). All chambers were sterilized by autoclaving before use.

Multicellular skin model biofabrication

The 3D tissue model was assembled from the bottom dermal matrix to the top epidermal layers. The dermal bioink, consisting of HDFs (10^5 cells/ml), fibrinogen (10 mg/ml; 341576, Millipore), aprotinin (0.025 mg/ml; A4529, Millipore), thrombin (1 U/ml; T7009, Millipore), and 10% (v/v) glycerol (G2025, Millipore) in Ca^{2+}-free DMEM, was deposited into a PDMS culture chamber with a 1-inch-long (2.54-cm-long), 30-gauge needle spanning the chamber (fig. S1, step 7). Upon gelation, an array of keratinocyte source droplets, containing GFP–E-cad–HaCaT cells (10^6 cells/ml) encapsulated in the fibrin

gel with the same formula as the dermal matrix, was bioprinted onto the dermal layer (2-mm center-to-center spacing) using a customized 3D printer (*30*, *78*, *79*). Notably, we selected the Ca^{2+}-free culture medium (residual calcium, 0.14 to 0.2 mM) to formulate bioinks for a slower fibrin gelation, ensuring smooth bioprinting before nozzle clotting.

Following fabrication, the tissue construct was cultured in DMEM-A for 10 to 14 days to allow self-organization of the epidermal layers. The metal needle was then removed to create a microchannel (fig. S1, step 8), which was endothelialized by HUVEC (10^7 cell/ml) suspension. After overnight incubation, the microchannel was washed with EGM-2 medium. Last, the culture chamber was transferred to a 35-mm dish (FB012920, Thermo Fisher Scientific) for continued tissue culture using EGM-2 (fig. S4). The culture medium was refreshed daily for an additional week.

3D matrix mechanical measurement

Matrix viscoelasticity was measured using a nanoindentor (iNano, KLA) equipped with a 500-μm flat punch tip. Four indentations were performed on each 3D matrix. The shear storage modulus (G') and loss modulus (G'') were obtained at a frequency of 60 Hz and 10% indentation depth. The complex shear modulus (G^*) was then calculated using the following equation

$$G^* = \sqrt{G'^2 + G''^2}$$

Diffusional permeability test

The barrier function of the endothelium and dermal stroma in regulating molecular diffusion was quantified by measuring the fluorescence intensity of 150-kDa FITC-dextran (74817, Sigma-Aldrich). Culture medium (EGM-2) containing dextran (10 μg/ml) was perfused through the built-in microchannel at a flow rate of 1 μl/min using a peristaltic pump (Reglo ICC 4-Channel, Ismatec) for 30 min. Time-lapse images were captured at 3-min intervals using a fluorescence microscope (THUNDER Imager, Leica). Image fluorescence intensity was quantified using ImageJ (https://imagej.net/ij/) with the Fiji processing package (https://fiji.sc/). The diffusional permeability coefficient (P_d), was then calculated using the following equation (*80*)

$$P_d = \frac{1}{I_0 - I_b}\left(\frac{I_t - I_0}{t}\right)\frac{d}{4}$$

where I_0 is the average initial intensity, I_b is the background intensity, I_t is the average intensity at time t (~30 min), t is the elapsed time, and d is the channel diameter.

PV induction and EGFR-targeted treatments

To induce desmosome disruption, AK23 (10 or 50 μg/ml; a PV antibody, D219-3, MBL Life Science) in EGM-2 medium was applied either directly onto the epidermis or via the side medium reservoirs. The latter allowed AK23 to diffuse through the endothelium and dermal stroma to reach the epidermal layers. EGFR-TKI treatments (osimertinib: S7297, lapatinib: S2111, and brigatinib: S8229, Selleck) were tested using both administration routes. Small-molecule agents were prepared by diluting their dimethyl sulfoxide stock solutions (1000×) in EGM-2 medium. Their efficacy in stabilizing desmosomal junctions was evaluated in the presence of AK23 (50 μg/ml) directly applied to the epidermis. Treated skin models were incubated on a rocking shaker (Rocker 2D, IKA) at 5 rpm with a 10° tilt for 24 hours before immunofluorescence assays. Details of the TKIs used are listed in table S3. Guided by their pharmacokinetics, the concentrations of osimertinib, lapatinib, and brigatinib were set at 0.126, 4.18, and 2.49 μM, respectively.

Immunofluorescence assays

Biofabricated skin constructs were visualized via whole-mount immunostaining. Skin models were fixed with 4% paraformaldehyde (PFA) in phosphate-buffered saline (PBS) for 2 hours, followed by 1 hour of permeabilization with 0.1% Triton X-100. Primary antibodies were introduced in a solution containing 1% bovine serum albumin (BSA) and glycine (22.52 mg/ml) in Dulbecco's PBS with 0.1% Tween 20. After overnight incubation at 4°C, samples were treated with secondary antibodies diluted in 1% BSA and incubated at 4°C for another 24 hours. Before imagining, nuclei were stained with DAPI. All samples were washed with PBS at least three times between each step described above.

Biofabricated tissues were also analyzed by staining cryosectioned slices. Skin constructs were first embedded in optimum cutting temperature compound within cryomolds and frozen in a cold isopentane bath cooled with dry ice pellets. Frozen tissues were cryosectioned at a thickness of 40 to 50 μm using a cryostat (CM1900, Lecia) at −20°C. Tissue slices were then thawed and fixed with 4% PFA in PBS for 10 min, followed by permeabilization with 0.1% Triton X-100 for 10 min and blocked for 1 hour. To visualize cell distribution and expression, primary and secondary antibodies (table S4) targeting individual biomarkers were sequentially applied to the slices. To assess PV antibody deposition and desmosomal junction integrity in the epidermis, slices from AK23-treated skin models were first incubated with secondary antibodies (anti-mouse) for 1 hour. Subsequently, Dsg3 was stained using primary and secondary antibodies. After DAPI staining, slices were mounted within ProLong Glass Antifade Mountant (P36984, Thermo Fisher Scientific) before imaging. The list of all primary and secondary antibodies used was provided in table S4. All frozen tissue samples were stored at −80°C

Fluorescence images were acquired using a tissue imager (THUNDER Imager, Leica) or a confocal microscope (LSM800, Zeiss) and analyzed with the Fiji processing package in ImageJ. The stained area percentage of COL-I and α-SMA was quantified to assess ECM deposition and HDF activation, respectively. AK23 fluorescence intensity was used to indicate antibody penetration, while the stained area ratio of AK23 to Dsg3 was calculated to evaluate their colocalization.

Cell-cell junction width measurement using FWHM

The analysis method was adapted from our previous study with further modifications (*37*). Briefly, a 10-pixel-thick reference line was drawn across two adjacent cell nuclei on a captured tissue slice image using ZEN blue software (ZEISS). Multichannel intensities, including E-cad and Dsg3, and their relative positions along the reference line were recorded and exported as Carl Zeiss Image files. The data were then batch processed using a custom MATLAB script. In the resulting 2D scatter plot of intensity (I) versus distance (X), the maximum (X_{max}) and minimum (X_{min}) distances corresponding to the half-maximum intensity ($I_{half\ max}$) were recorded. The difference between X_{max} and X_{min}, referred to as the FWHM, was calculated to represent the width of the cell-cell junction, as illustrated in fig. S11.

EGFR-TKI efficacy quantification based on individual junction width

The efficacy of EGFR-TKI treatment was calculated on the basis of the relative change of cell-cell junction width (FWHM value), comparing TKI-treated samples with healthy and PV controls, using the following equation

$$\text{Efficacy} = \frac{\text{FWHM}_{\text{TKI}} - \text{FWHM}_{\text{PV}}}{\text{FWHM}_{\text{Healthy}} - \text{FWHM}_{\text{PV}}} \times 100\,\%$$

ML-assisted tissue slice analysis

Grayscale images of tissue microsections (red Dsg3 channel) were analyzed using MATLAB toolboxes (Statistical and Machine Learning; Image Processing) to extract texture features. To capture local textures, each image (512 pixels by 512 pixels) was subdivided into sixteen 128 pixel–by–128 pixel subimages. To eliminate background noise and cytosolic regions, subimages in which ≥80% of the pixels had intensities below 5% of the maximum image intensity were excluded from further analysis. Texture features were quantified using GLCM analysis. Specifically, correlation (measuring the dependency of pixel intensities over a defined distance) and SD (a measure of variation in intensity values) were calculated for each subimage after normalizing pixel intensities to the maximum value within the image. The texture parameters for each tissue slice image were obtained by averaging the corresponding values from all valid subimages.

To evaluate the therapeutic efficacy of EGFR-TKIs, a Random Forest algorithm was implemented in R. The ML model included 300 decision trees and was optimized using a fivefold cross-validation approach. Training and testing data consisted of texture parameters extracted from two control groups: untreated healthy skin models and PV models induced by topical application of AK23 (50 μg/ml). Eighty percent of the dataset was allocated for model training, and the remaining 20% was reserved for testing. The ML model achieved over 80% accuracy in distinguishing between the two distinct model types. Texture features from TKI-treated models were subsequently input into the trained ML model to assess their classification relative to the control groups. The list of sample sizes used for training and treatment prediction in the ML-assisted analysis is provided in table S1.

Statistical analysis

All data in plots and bar charts were presented as quantitative values, shown as means ± SD, unless otherwise stated in the figure captions. Statistical analyses were performed and plotted using OriginPro. Outliers were removed using the interquartile range method when analyzing cell-cell junction width. Statistical significance between two groups was calculated using Student's t test. A P value less than 0.05 was considered statistically significant ($^*P < 0.05$, $^{**}P < 0.01$, and $^{***}P < 0.001$). Cohen's κ was used to statistically assess the agreement between automated and manual analyses.

Supplementary Materials

The PDF file includes:

Figs. S1 to S17
Tables S1 to S4
Legends for codes S1 and S2

Other Supplementary Material for this manuscript includes the following:

Codes S1 and S2

REFERENCES

1. A. H. Abend, I. He, N. Bahroos, S. Christianakis, A. B. Crew, L. M. Wise, G. P. Lipori, X. He, S. N. Murphy, C. D. Herrick, J. Avasarala, M. G. Weiner, J. S. Zelko, E. Matute-Arcos, M. Abajian, P. R. Payne, A. M. Lai, H. A. Davis, A. A. Hoberg, C. E. Ortman, A. D. Gode, B. W. Taylor, K. I. Osinski, D. N. Di Florio, N. R. Rose, F. W. Miller, G. C. Tsokos, D. L. Fairweather, Estimation of prevalence of autoimmune diseases in the United States using electronic health record data. *J. Clin. Invest.* **135**, e178722 (2025).
2. M. D. Rosenblum, I. K. Gratz, J. S. Paw, A. K. Abbas, Treating human autoimmunity: Current practice and future prospects. *Sci. Transl. Med.* **4**, 125sr1 (2012).
3. L. Fugger, L. T. Jensen, J. Rossjohn, Challenges, progress, and prospects of developing therapies to treat autoimmune diseases. *Cell* **181**, 63–80 (2020).
4. M. Kasperkiewicz, C. T. Ellebrecht, H. Takahashi, J. Yamagami, D. Zillikens, A. S. Payne, M. Amagai, Pemphigus. *Nat. Rev. Dis. Primers* **3**, 17026 (2017).
5. M. G. Mahoney, Z. Wang, K. Rothenberger, P. J. Koch, M. Amagai, J. R. Stanley, Explanations for the clinical and microscopic localization of lesions in pemphigus foliaceus and vulgaris. *J. Clin. Invest.* **103**, 461–468 (1999).
6. K. Schulze, A. Galichet, B. S. Sayar, A. Scothern, D. Howald, H. Zymann, M. Siffert, D. Zenhäusern, R. Bolli, P. J. Koch, D. Garrod, M. M. Suter, E. J. Müller, An adult passive transfer mouse model to study desmoglein 3 signaling in pemphigus vulgaris. *J. Invest. Dermatol.* **132**, 346–355 (2012).
7. I. Sánchez-Carpintero, A. España, B. Pelacho, N. López Moratalla, D. S. Rubenstein, L. A. Diaz, M. J. López-Zabalza, In vivo blockade of pemphigus vulgaris acantholysis by inhibition of intracellular signal transduction cascades. *Br. J. Dermatol.* **151**, 565–570 (2004).
8. M. Bektas, P. S. Jolly, P. Berkowitz, M. Amagai, D. S. Rubenstein, A pathophysiologic role for epidermal growth factor receptor in pemphigus acantholysis. *J. Biol. Chem.* **288**, 9447–9456 (2013).
9. H. Franz, M. Rathod, A. Zimmermann, C. Stüdle, V. Beyersdorfer, K. Leal-Fischer, P. Hanns, T. Cunha, D. Didona, M. Hertl, M. Scheibe, F. Butter, E. Schmidt, V. Spindler, Unbiased screening identifies regulators of cell-cell adhesion and treatment options in pemphigus. *Nat. Commun.* **15**, 8044 (2024).
10. B. Kaur, J. Kerbrat, J. Kho, M. Kaler, S. Kanatsios, N. Cirillo, Mechanism-based therapeutic targets of pemphigus vulgaris: A scoping review of pathogenic molecular pathways. *Exp. Dermatol.* **31**, 154–171 (2022).
11. P. Berkowitz, P. Hu, S. Warren, Z. Liu, L. A. Diaz, D. S. Rubenstein, p38MAPK inhibition prevents disease in pemphigus vulgaris mice. *Proc. Natl. Acad. Sci. U.S.A.* **103**, 12855–12860 (2006).
12. B. S. Sayar, S. Rüegg, E. Schmidt, M. Sibilia, M. Siffert, M. M. Suter, A. Galichet, E. J. Müller, EGFR inhibitors erlotinib and lapatinib ameliorate epidermal blistering in pemphigus vulgaris in a non-linear, V-shaped relationship. *Exp. Dermatol.* **23**, 33–38 (2014).
13. D. T. Egu, T. Schmitt, N. Ernst, R. J. Ludwig, M. Fuchs, M. Hiermaier, S. Moztarzadeh, C. S. Morón, E. Schmidt, V. Beyersdorfer, V. Spindler, L. S. Steinert, F. Vielmuth, A. M. Sigmund, J. Waschke, EGFR inhibition by erlotinib rescues desmosome ultrastructure and keratin anchorage and protects against pemphigus vulgaris IgG–induced acantholysis in human epidermis. *J. Invest. Dermatol.* **144**, 2440–2452 (2024).
14. A. M. Sigmund, M. Winkler, S. Engelmayer, D. Kugelmann, D. T. Egu, L. S. Steinert, M. Fuchs, M. Hiermaier, M. Y. Radeva, F. C. Bayerbach, E. Butz, S. Kotschi, C. Hudemann, M. Hertl, S. Yeruva, E. Schmidt, A. S. Yazdi, K. Ghoreschi, F. Vielmuth, J. Waschke, Apremilast prevents blistering in human epidermis and stabilizes keratinocyte adhesion in pemphigus. *Nat. Commun.* **14**, 116 (2023).
15. G. van der Wier, H. H. Pas, M. F. Jonkman, Experimental human cell and tissue models of pemphigus. *Dermatol. Res. Pract.* **2010**, 143871 (2010).
16. I. A. K. Burmester, S. Flaswinkel, C.-S. Thies, A. Kasprick, M. Kamaguchi, V. Bumiller-Bini, S. Emtenani, N. Feldmann, K. Kridin, E. Schmidt, N. van Beek, D. Zillikens, C. M. Hammers, J. E. Hundt, R. J. Ludwig, Identification of novel therapeutic targets for blocking acantholysis in pemphigus. *Br. J. Pharmacol.* **177**, 5114–5130 (2020).
17. X. Jin, J. Rosenbohm, E. Kim, A. M. Esfahani, K. Seiffert-Sinha, J. K. Wahl III, J. Y. Lim, A. A. Sinha, R. Yang, Modulation of mechanical stress mitigates anti-Dsg3 antibody-induced dissociation of cell–cell adhesion. *Adv. Biol.* **5**, e2000159 (2021).
18. G. J. Anhalt, R. S. Labib, J. J. Voorhees, T. F. Beals, L. A. Diaz, Induction of pemphigus in neonatal mice by passive transfer of IgG from patients with the disease. *N. Engl. J. Med.* **306**, 1189–1196 (1982).
19. M. Amagai, K. Tsunoda, H. Suzuki, K. Nishifuji, S. Koyasu, T. Nishikawa, Use of autoantigen-knockout mice in developing an active autoimmune disease model for pemphigus. *J. Clin. Invest.* **105**, 625–631 (2000).
20. Y. Takae, T. Nishikawa, M. Amagai, Pemphigus mouse model as a tool to evaluate various immunosuppressive therapies. *Exp. Dermatol.* **18**, 252–260 (2009).
21. A. I. Minchinton, I. F. Tannock, Drug penetration in solid tumours. *Nat. Rev. Cancer* **6**, 583–592 (2006).
22. M. J. Eigenmann, T. V. Karlsen, B.-F. Krippendorff, O. Tenstad, L. Fronton, M. B. Otteneder, H. Wiig, Interstitial IgG antibody pharmacokinetics assessed by combined in vivo- and

physiologically-based pharmacokinetic modelling approaches. *J. Physiol.* **595**, 7311–7330 (2017).
23. F. Pampaloni, E. G. Reynaud, E. H. K. Stelzer, The third dimension bridges the gap between cell culture and live tissue. *Nat. Rev. Mol. Cell Biol.* **8**, 839–845 (2007).
24. M. A. Skylar-Scott, S. G. M. Uzel, L. L. Nam, J. H. Ahrens, R. L. Truby, S. Damaraju, J. A. Lewis, Biomanufacturing of organ-specific tissues with high cellular density and embedded vascular channels. *Sci. Adv.* **5**, eaaw2459 (2019).
25. H.-J. Stark, M. Baur, D. Breitkreutz, N. Mirancea, N. E. Fusenig, Organotypic keratinocyte cocultures in defined medium with regular epidermal morphogenesis and differentiation. *J. Invest. Dermatol.* **112**, 681–691 (1999).
26. B. Morgner, J. Tittelbach, C. Wiegand, Induction of psoriasis- and atopic dermatitis-like phenotypes in 3D skin equivalents with a fibroblast-derived matrix. *Sci. Rep.* **13**, 1807 (2023).
27. H.-W. Kang, S. J. Lee, I. K. Ko, C. Kengla, J. J. Yoo, A. Atala, A 3D bioprinting system to produce human-scale tissue constructs with structural integrity. *Nat. Biotechnol.* **34**, 312–319 (2016).
28. C. Mota, S. Camarero-Espinosa, M. B. Baker, P. Wieringa, L. Moroni, Bioprinting: From tissue and organ development to in vitro models. *Chem. Rev.* **120**, 10547–10607 (2020).
29. I. K. Zervantonakis, S. K. Hughes-Alford, J. L. Charest, J. S. Condeelis, F. B. Gertler, R. D. Kamm, Three-dimensional microfluidic model for tumor cell intravasation and endothelial barrier function. *Proc. Natl. Acad. Sci. U.S.A.* **109**, 13515–13520 (2012).
30. F. Meng, C. M. Meyer, D. Joung, D. A. Vallera, M. C. McAlpine, A. Panoskaltsis-Mortari, 3D bioprinted in vitro metastatic models via reconstruction of tumor microenvironments. *Adv. Mater.* **31**, e1806899 (2019).
31. V. Lee, G. Singh, J. P. Trasatti, C. Bjornsson, X. Xu, T. N. Tran, S.-S. Yoo, G. Dai, P. Karande, Design and fabrication of human skin by three-dimensional bioprinting. *Tissue Eng. Part C Methods* **20**, 473–484 (2014).
32. M. Albanna, K. W. Binder, S. V. Murphy, J. Kim, S. A. Qasem, W. Zhao, J. Tan, I. B. El-Amin, D. D. Dice, J. Marco, J. Green, T. Xu, A. Skardal, J. H. Holmes, J. D. Jackson, A. Atala, J. J. Yoo, In situ bioprinting of autologous skin cells accelerates wound healing of extensive excisional full-thickness wounds. *Sci. Rep.* **9**, 1856 (2019).
33. B. S. Kim, M. Ahn, W.-W. Cho, G. Gao, J. Jang, D.-W. Cho, Engineering of diseased human skin equivalent using 3D cell printing for representing pathophysiological hallmarks of type 2 diabetes in vitro. *Biomaterials* **272**, 120776 (2021).
34. A. K. Miri, I. Mirzaee, S. Hassan, S. Mesbah Oskui, D. Nieto, A. Khademhosseini, Y. S. Zhang, Effective bioprinting resolution in tissue model fabrication. *Lab Chip* **19**, 2019–2037 (2019).
35. T. Lechler, E. Fuchs, Asymmetric cell divisions promote stratification and differentiation of mammalian skin. *Nature* **437**, 275–280 (2005).
36. S. Ipponjima, T. Hibi, T. Nemoto, Three-dimensional analysis of cell division orientation in epidermal basal layer using intravital two-photon microscopy. *PLoS One* **11**, e0163199 (2016).
37. H. Zhai, X. Jin, G. Minnick, J. Rosenbohm, M. A. H. Hafiz, R. Yang, F. Meng, Spatially guided construction of multilayered epidermal models recapturing structural hierarchy and cell–cell junctions. *Small Sci.* **2**, 2200051 (2022).
38. Y. A. Miroshnikova, H. Q. Le, D. Schneider, T. Thalheim, M. Rübsam, N. Bremicker, J. Polleux, N. Kamprad, M. Tarantola, I. Wang, M. Balland, C. M. Niessen, J. Galle, S. A. Wickström, Adhesion forces and cortical tension couple cell proliferation and differentiation to drive epidermal stratification. *Nat. Cell Biol.* **20**, 69–80 (2018).
39. E. Proksch, J. M. Brandner, J.-M. Jensen, The skin: An indispensable barrier. *Exp. Dermatol.* **17**, 1063–1072 (2008).
40. A. Meana, J. Iglesias, M. Del Rio, F. Larcher, B. Madrigal, M. F. Fresno, C. Martin, F. San Roman, F. Tevar, Large surface of cultured human epithelium obtained on a dermal matrix based on live fibroblast-containing fibrin gels. *Burns* **24**, 621–630 (1998).
41. M. J. Helmedag, S. Weinandy, Y. Marquardt, J. M. Baron, N. Pallua, C. V. Suschek, S. Jockenhoevel, The effects of constant flow bioreactor cultivation and keratinocyte seeding densities on prevascularized organotypic skin grafts based on a fibrin scaffold. *Tissue Eng. Part A* **21**, 343–352 (2015).
42. L. Goers, P. Freemont, K. M. Polizzi, Co-culture systems and technologies: Taking synthetic biology to the next level. *J. R. Soc. Interface* **11**, 20140065 (2014).
43. S.-H. Kim, Y. Song, H. R. Seo, GSK-3β regulates the endothelial-to-mesenchymal transition via reciprocal crosstalk between NSCLC cells and HUVECs in multicellular tumor spheroid models. *J. Exp. Clin. Cancer Res.* **38**, 46 (2019).
44. T. Chen, B. Zhang, H. Xie, C. Huang, Q. Wu, GRHL2 regulates keratinocyte EMT-MET dynamics and scar formation during cutaneous wound healing. *Cell Death Dis.* **15**, 748 (2024).
45. J. W. O'Connor, K. Mistry, D. Detweiler, C. Wang, E. W. Gomez, Cell-cell contact and matrix adhesion promote αSMA expression during TGFβ1-induced epithelial-myofibroblast transition via Notch and MRTF-A. *Sci. Rep.* **6**, 26226 (2016).
46. J. R. Bezenah, Y. P. Kong, A. J. Putnam, Evaluating the potential of endothelial cells derived from human induced pluripotent stem cells to form microvascular networks in 3D cultures. *Sci. Rep.* **8**, 2671 (2018).
47. S.-C. Lee, J.-B. Lee, J.-P. Kook, J.-J. Seo, Y. P. Kim, K.-I. Nam, S.-S. Park, Expression of differentiation markers during fetal skin development in humans: Immunohistochemical studies on the precursor proteins forming the cornified cell envelope. *J. Invest. Dermatol.* **112**, 882–886 (1999).
48. T. Kihara, J. Ito, J. Miyake, Measurement of biomolecular diffusion in extracellular matrix condensed by fibroblasts using fluorescence correlation spectroscopy. *PLoS One* **8**, e82382 (2013).
49. C. F. Hung, M. G. Rohani, S.-S. Lee, P. Chen, L. M. Schnapp, Role of IGF-1 pathway in lung fibroblast activation. *Respir. Res.* **14**, 102 (2013).
50. D. M. Dolivo, S. A. Larson, T. Dominko, FGF2-mediated attenuation of myofibroblast activation is modulated by distinct MAPK signaling pathways in human dermal fibroblasts. *J. Dermatol. Sci.* **88**, 339–348 (2017).
51. R. Belvedere, N. Novizio, S. Morello, A. Petrella, The combination of mesoglycan and VEGF promotes skin wound repair by enhancing the activation of endothelial cells and fibroblasts and their cross-talk. *Sci. Rep.* **12**, 11041 (2022).
52. S. Cao, Y. Pan, A. S. Terker, J. P. Arroyo Ornelas, Y. Wang, J. Tang, A. Niu, S. A. Kar, M. Jiang, W. Luo, X. Dong, X. Fan, S. Wang, M. H. Wilson, A. Fogo, M.-Z. Zhang, R. C. Harris, Epidermal growth factor receptor activation is essential for kidney fibrosis development. *Nat. Commun.* **14**, 7357 (2023).
53. R. Oftadeh, M. Azadi, M. Donovan, J. Langer, I.-C. Liao, C. Ortiz, A. J. Grodzinsky, G. S. Luengo, Poroelastic behavior and water permeability of human skin at the nanoscale. *PNAS Nexus* **2**, pgad240 (2023).
54. L. Claesson-Welsh, E. Dejana, D. M. McDonald, Permeability of the endothelial barrier: Identifying and reconciling controversies. *Trends Mol. Med.* **27**, 314–331 (2021).
55. I. A. K. Burmester, S. Emtenani, J.-G. Johns, R. J. Ludwig, C. M. Hammers, J. E. Hundt, Translational use of a standardized full human skin organ culture model in autoimmune blistering diseases. *Curr. Protoc. Pharmacol.* **85**, e56 (2019).
56. V. Hartmann, W. V. Hariton, S. Rahimi, C. M. Hammers, R. J. Ludwig, E. J. Müller, J. E. Hundt, The human skin organ culture model as an optimal complementary tool for murine pemphigus models. *Lab. Anim.* **57**, 381–395 (2023).
57. S. Ono, G. Egawa, T. Nomura, A. Kitoh, T. Dainichi, A. Otsuka, S. Nakajima, M. Amagai, F. Matsumoto, M. Yamamoto, Y. Kubota, T. Takai, T. Honda, K. Kabashima, Abl family tyrosine kinases govern IgG extravasation in the skin in a murine pemphigus model. *Nat. Commun.* **10**, 4432 (2019).
58. K. R. Feingold, Thematic review series: Skin lipids. The role of epidermal lipids in cutaneous permeability barrier homeostasis. *J. Lipid Res.* **48**, 2531–2546 (2007).
59. V. Rötzer, E. Hartlieb, F. Vielmuth, M. Gliem, V. Spindler, J. Waschke, E-cadherin and Src associate with extradesmosomal Dsg3 and modulate desmosome assembly and adhesion. *Cell. Mol. Life Sci.* **72**, 4885–4897 (2015).
60. M. Amagai, P. J. Koch, T. Nishikawa, J. R. Stanley, Pemphigus vulgaris antigen (desmoglein 3) is localized in the lower epidermis, the site of blister formation in patients. *J. Invest. Dermatol.* **106**, 351–355 (1996).
61. D. A. E. Cross, S. E. Ashton, S. Ghiorghiu, C. Eberlein, C. A. Nebhan, P. J. Spitzler, J. P. Orme, M. R. V. Finlay, R. A. Ward, M. J. Mellor, G. Hughes, A. Rahi, V. N. Jacobs, M. R. Brewer, E. Ichihara, J. Sun, H. Jin, P. Ballard, K. Al-Kadhimi, R. Rowlinson, T. Klinowska, G. H. P. Richmond, M. Cantarini, D.-W. Kim, M. R. Ranson, W. Pao, AZD9291, an irreversible EGFR TKI, overcomes T790M-mediated resistance to EGFR inhibitors in lung cancer. *Cancer Discov.* **4**, 1046–1061 (2014).
62. A. J. Tevaarwerk, J. M. Kolesar, Lapatinib: A small-molecule inhibitor of epidermal growth factor receptor and human epidermal growth factor receptor—2 tyrosine kinases used in the treatment of breast cancer. *Clin. Ther.* **31**, 2332–2348 (2009).
63. M. Ceccon, L. Mologni, W. Bisson, L. Scapozza, C. Gambacorti-Passerini, Crizotinib-resistant NPM-ALK mutants confer differential sensitivity to unrelated Alk inhibitors. *Mol. Cancer Res.* **11**, 122–132 (2013).
64. A. Wibmer, H. Hricak, T. Gondo, K. Matsumoto, H. Veeraraghavan, D. Fehr, J. Zheng, D. Goldman, C. Moskowitz, S. W. Fine, V. E. Reuter, J. Eastham, E. Sala, H. A. Vargas, Haralick texture analysis of prostate MRI: Utility for differentiating non-cancerous prostate from prostate cancer and differentiating prostate cancers with different Gleason scores. *Eur. Radiol.* **25**, 2840–2850 (2015).
65. A. Sarica, A. Cerasa, A. Quattrone, Random forest algorithm for the classification of neuroimaging data in Alzheimer's disease: A systematic review. *Front. Aging Neurosci.* **9**, 329 (2017).
66. M. L. McHugh, Interrater reliability: The kappa statistic. *Biochem. Med.* **22**, 276–282 (2012).
67. M. Xue, C. J. Jackson, Extracellular matrix reorganization during wound healing and its impact on abnormal scarring. *Adv. Wound Care* **4**, 119–136 (2015).
68. M. Wufuer, G. Lee, W. Hur, B. Jeon, B. J. Kim, T. H. Choi, S. Lee, Skin-on-a-chip model simulating inflammation, edema and drug-based treatment. *Sci. Rep.* **6**, 37471 (2016).
69. T. Funakoshi, L. Lunardon, C. T. Ellebrecht, A. R. Nagler, C. E. O'Leary, A. S. Payne, Enrichment of total serum IgG4 in patients with pemphigus. *Br. J. Dermatol.* **167**, 1245–1253 (2012).
70. C. T. Ellebrecht, D. Maseda, A. S. Payne, Pemphigus and pemphigoid: From disease mechanisms to druggable pathways. *J. Invest. Dermatol.* **142**, 907–914 (2022).

71. R. Shah, J. F. Lester, Tyrosine kinase inhibitors for the treatment of EGFR mutation-positive non–small-cell lung cancer: A clash of the generations. *Clin. Lung Cancer* **21**, e216–e228 (2020).
72. M. Chen, Z. Xu, Y. Chen, Q. Yang, R. Lu, Y. Dong, X. Li, J. Xie, R.-H. Xu, H. Jia, Y. Kang, Y. Wu, EGFR marks a subpopulation of dermal mesenchymal cells highly expressing IGF1 which enhances hair follicle regeneration. *J. Cell Mol. Med.* **27**, 1697–1707 (2023).
73. C.-Y. Cheng, S.-H. Hsu, U. Chokkalingam, Y.-S. Dai, P.-C. Shih, P. Ekambaranellore, W.-W. Lin, Aloe polysaccharide promotes keratinocyte proliferation, migration, and differentiation by upregulating the EGFR/PKC-dependent signaling pathways. *Sci. Rep.* **15**, 8196 (2025).
74. C. Vasavda, B. K. Ho, D. Y. Zhang, K. A. Williams, B. H. Kaffenberger, S. G. Kwatra, M. M. Kwatra, First- and third-generation epidermal growth factor receptor inhibitors mediate distinct phosphoprotein signalling networks: Implications for adverse dermatological reactions. *Br. J. Dermatol.* **183**, 1105–1107 (2020).
75. T. Waghule, G. Singhvi, S. K. Dubey, M. M. Pandey, G. Gupta, M. Singh, K. Dua, Microneedles: A smart approach and increasing potential for transdermal drug delivery system. *Biomed. Pharmacother.* **109**, 1249–1258 (2019).
76. S. Maity, I. Banerjee, R. Sinha, H. Jha, P. Ghosh, S. Mustafi, Nikolsky's sign: A pathognomic boon. *J. Family Med. Prim. Care* **9**, 526–530 (2020).
77. J. A. Bouwstra, R. W. J. Helder, A. El Ghalbzouri, Human skin equivalents: Impaired barrier function in relation to the lipid and protein properties of the stratum corneum. *Adv. Drug Deliv. Rev.* **175**, 113802 (2021).
78. M. K. Gupta, F. Meng, B. N. Johnson, Y. L. Kong, L. Tian, Y.-W. Yeh, N. Masters, S. Singamaneni, M. C. McAlpine, 3D printed programmable release capsules. *Nano Lett.* **15**, 5321–5329 (2015).
79. D. Joung, V. Truong, C. C. Neitzke, S.-Z. Guo, P. J. Walsh, J. R. Monat, F. Meng, S. H. Park, J. R. Dutton, A. M. Parr, M. C. McAlpine, 3D printed stem-cell derived neural progenitors generate spinal cord scaffolds. *Adv. Funct. Mater.* **28**, 1801850 (2018).
80. D. B. Kolesky, K. A. Homan, M. A. Skylar-Scott, J. A. Lewis, Three-dimensional bioprinting of thick vascularized tissues. *Proc. Natl. Acad. Sci. U.S.A.* **113**, 3179–3184 (2016).

Acknowledgments: We thank the Nano-Engineering Research Core Facility (NERCF) and Light & Electron Microscopy Core (LEMC) at the University of Nebraska-Lincoln for the assistance in sample preparation and characterization. **Funding:** This work was funded by the following organizations: National Institutes of Health, National Institute of General Medical Sciences grant P20 GM113126, Nebraska Center for Integrated Biomolecular Communication (to F.M.); Nebraska Tobacco Settlement Biomedical Research Development Funds (to F.M.); American Cancer Society grant IRG-22-146-07-IRG (to F.M.); National Institutes of Health, National Cancer Institute grant CA036727, Buffett Cancer Center (to F.M.); Nexus of Virology, Immunology, and Bioengineering (to F.M.); Voelte-Keegan Bioengineering Support (to F.M.); National Science Foundation grant nos. 1826135, 2143997, 2450416, and 2503605 (to R.Y.); and National Institutes of Health, National Institute of General Medical Sciences grant R35 GM150623 (to R.Y.). **Author contributions:** Conceptualization: F.M., R.Y., H.Z., and K.S.-S. Methodology: F.M., H.Z., and R.Y. Software: A.O.M. and H.Z. Validation: H.Z., F.M., R.Y., and X.J. Formal analysis: F.M., H.Z., R.Y., A.A.S., X.J., and A.O.M. Investigation: H.Z., X.J., M.F.S., and R.Y. Resources: F.M., R.Y., H.Z., K.S.-S., and X.J. Data curation: H.Z., F.M., and R.Y. Writing—original draft: F.M., H.Z., and R.Y. Writing—review and editing: F.M., R.Y., K.S.-S., H.Z., A.A.S., A.O.M., and X.J. Visualization: H.Z., A.O.M., R.Y., and X.J. Supervision: F.M. and R.Y. Project administration: F.M. and R.Y. Funding acquisition: F.M. and R.Y. **Competing interests:** F.M., R.Y., H.Z., and X.J. are inventors on a patent application entitled "Three-dimensional skin constructs" related to this work filed on 11 September 2024, with application number 18/830,822. The authors declare that they have no other competing interests. **Data and materials availability:** All data and code needed to evaluate and reproduce the results in the paper are present in the paper and/or the Supplementary Materials. Additional supporting data and microscope images are available at the Data Repository for the University of Nebraska-Lincoln (https://doi.org/10.71964/121).

Submitted 3 June 2025
Accepted 11 December 2025
Published 9 January 2026
10.1126/sciadv.adz5003